INVESTIGATION OF ELECTRONIC, VIBRATIONAL, MECHANIC AND CHEMICAL PROPERTIES OF 2D-DLHC CuI CRYSTAL

A Thesis Submitted to
the Graduate School of Engineering and Sciences of
İzmir Institute of Technology
in Partial Fulfillment of the Requirements for the Degree of

MASTER OF SCIENCE

in Chemistry

by
Ali Cem DEMİROK

July 2023
İZMİR

We approve the thesis of **Ali Cem DEMİROK**

Asst. Prof. Dr. Onur BÜYÜKÇAKIR
Department of Chemistry, İzmir Institute of Technology

Prof. Dr. Hasan ŞAHİN
Department of Photonics, İzmir Institute of Technology

Assoc. Prof. Dr. Mehmet YAĞMURCUKARDEŞ
Department of Photonics, İzmir Institute of Technology

Assoc. Prof. Dr. Serkan ATEŞ
Department of Physics, İzmir Institute of Technology

Assoc. Prof. Dr. Ümit AKINCI
Department of Physics, Dokuz Eylül University

4 July 2023

Asst. Prof. Dr. Onur Büyükçakır
Supervisor, Department of Chemistry
İzmir Institute of Technology

Prof. Dr. Hasan Şahin
Co-Supervisor, Department of Photonics
İzmir Institute of Technology

Prof. Dr. Gülşah ŞANLI-MOHAMED
Head of the Department of
Chemistry

Prof. Dr. Mehtap EANES
Dean of the Graduate School of
Engineering and Sciences

ACKNOWLEDGMENTS

I need to show my biggest gratitude to my co-supervisor Prof. Dr. Hasan Şahin. In both my undergraduate and graduate studies, he taught me the importance of work ethic, time management and teamwork. At the same time, I would like to thank Asst. Prof. Dr. Onur Büyükçakır and Assoc. Prof. Mehmet Yağmurcukardeş for all of his academic assistance.

I would like to send a note of thanks to the members of the CENT group, Yiğit Sözen, Mehmet Başkurt, Yankı Öncü Yayak, Onur Ercem, Tuna Duran, Fırat Tan, Tayfun Kutlu, and Ozan Orhan. Working with you every day has been a wonderful experience.

Then there's my brother and my father. I can't express my gratitude to you enough for your love, assistance, and numerous other unfathomable gifts. No matter what the circumstances, you have always been there for me.

ABSTRACT

INVESTIGATION OF ELECTRONIC, VIBRATIONAL, MECHANIC AND CHEMICAL PROPERTIES OF 2D-DLHC CuI CRYSTAL

The branch of material science and nanotechnology has recently seen the emergence of a remarkable class of materials known as 2D materials. These materials have unusual features and behaviours because of their special two-dimensional structure that separates them apart from bulk materials. One of the characteristics of 2D materials are related to their capacity to handle large mechanical deformation without fracture. Since the discovery of graphene, researchers have discovered and created an extensive range of additional 2D materials with a variety of chemical compositions and topologies. These materials can be used for energy storage, sensing, catalysis and biomedical applications.

In this thesis, electronic, vibrational, mechanic and chemical properties of single-layer CuI were investigated by using density functional theory (DFT) based first-principles calculations. It is shown that the CuI structure crystallizes in a hexagonal lattice by energy and geometry optimizations. The vibrational properties of the material were examined by phonon and Raman calculations and the structure found to be dynamically stable and there were four Raman active modes. The electronic band dispersions and corresponding density of states showed that the single-layer CuI crystal has semiconductor nature with direct band gap. Strain calculations were performed to examine the mechanical strength of the CuI crystal. Effect of biaxial strain on the electronic band structure of CuI crystal was investigated in the range of $\pm 5\%$ and the direct band gap behaviour did not change. Biaxial and uniaxial strain calculations have shown that it is resistant to high stresses.

ÖZET

İKİ BOYUTLU CuI KRİSTALİNİN ELEKTRONİK, TİTREŞİMSEL, MEKANİK VE KİMYASAL ÖZELLİKLERİNİN İNCELENMESİ

Son zamanlarda (2B) iki boyutlu malzemeler olarak bilinen dikkate değer bir malzeme sınıfının ortaya çıkışı, malzeme bilimi ve nanoteknolojik çalışmalar için ilgi görmüştür. Bu malzemeler, onları yığın malzemelerden ayıran özel iki boyutlu yapılarından dolayı alışılmadık özelliklere ve davranışlara sahiptir. İki boyutlu malzemelerin özelliklerinden biri, yüksek mekanik deformasyonlara karşı kırılma olmaksızın dayanabilme kapasiteleridir. Grafenin keşfinden sonra, araştırmacılar, çeşitli kimyasal bileşimler ve topolojilere sahip çok çeşitli iki boyutlu malzemeler sentezlediler. Keşfedimiş yeni malzemeler, sektörde, enerji depolama, algılama, kataliz ve biyomedikal uygulamalarda kullanılabilir.

Bu tezde, tek katmanlı CuI'nın yapısal, elektronik, titreşimsel ve mekanik özellikleri, yoğunluk fonksiyonel teorisi (DFT) kullanılarak incelenmiştir. Öncelikle CuI kristalinin altıgen bir yapıda kristalleştiği, enerji ve geometri optimizasyonları ile gösterilmiştir. Malzemenin titreşimsel özellikleri fonon ve Raman hesaplamaları ile incelenip, yapının dinamik olarak kararlı olduğu ve gama noktasında 4 adet Raman aktif modunun olduğu anlaşılmıştır. Elektronik bant dağınımları ve karşılık gelen durum yoğunluğu grafikleri, tek katmanlı CuI kristalinin doğrudan bant aralığı ve yarı iletken doğasına sahip olduğunu göstermiştir. CuI kristalinin mekanik dayanımını incelemek için germe hesaplamaları yapılmıştır. Çift eksenli gerilimin, CuI kristalinin elektronik bant yapısı üzerindeki etkisi $\pm 5\%$ aralığında incelenmiştir ve doğrudan bant aralığı davranışı değişmemiştir. Çift eksenli ve tek eksenli germe hesapları, bu malzemenin yüksek gerilmelere karşı dayanıklı olduğunu göstermiştir.

TABLE OF CONTENTS

LIST OF FIGURES

Figure **Page**

LIST OF TABLES

Table **Page**

CHAPTER 1

INTRODUCTION

Copper iodide is an inorganic compound with the formula CuI. Also known as coprous iodide in the literature. Copper iodide which has a white color, can also be seen in skin color in some samples. CuI occurs in nature as a rare mineral. The mineral is called marshite has a reddish-brown color. Copper iodide has been synthesized over the years using a variety of methods. The first large-scale synthesis of copper iodide has been known and studied for so long that it is difficult to pinpoint an exact date. Copper iodide was probably first synthesized in the early 19th century. Bulk copper iodide was synthesized by heating iodine and copper in concentrated hydriodic acid[65].

Extensive research has been conducted to better investigate the behavior of copper iodide and its potential in fields such as electronics, optoelectronics[10], photovoltaics[88], and heterogeneous catalysis[87]. Investigation of copper iodide's crystal structure, phase transitions, and thermal properties, which are essential in predicting its performance and behavior under various circumstances, has required a large investment of research time. Additionally, different synthetic pathways and growth methods have been investigated to modify copper iodide's physical features, enabling the fine-tuning of its properties to match certain application needs. Using bulk copper iodide particles in nanoscale electronics and composite materials has been used new applications thanks to the ability to tune their morphology, size, and surface properties[70,106,44,61,20].

The crystal structure, phase purity and lattice characteristics was ascertained using X-ray diffraction (XRD)[7,40,42]. It is possible to learn more about the morphology, particle size distribution, and surface characteristics of the produced copper iodide by using scanning electron microscopy (SEM)[106,97,64] and transmission electron microscopy (TEM)[40]. The identification of chemical bonds and functional groups in the material can be investigate easier by spectroscopic methods like Fourier-transform infrared (FTIR) and Raman spectroscopy.[40,86]

In 2004, Novoselov and his colleagues discovered graphene which the first isolated 2D material[77]. Researchers have been interested in atomic scale-thick materials due to their potential as building blocks for quantum devices. Because of quantum effects in 2D, electronic behavior differs from that in 3D, bringing remarkable qualities that must be investigated.

Since the emergence of remarkable electrical and mechanical properties in graphene in comparison to its bulk forms, researchers have been focused on the exploration of outstanding physics in graphene[27]. The sp^2 hybridization between the C atoms that form the hexagonal lattice provides high in-plane stiffness, Young's modulus, and strength[54], when the bonds between the delocalized electrons in p_z orbitals lead to the Dirac cone formation at the Fermi level, where charge carriers behave like massless fermions at low-excitations, revealing graphene's high electrical and thermal conductivity[76,75,9]. As a consequence of these remarkable characteristics of graphene has provided the way for the development of more compact and advanced devices that can be used in a wide range of technology applications such as nanoelectronics[46,58], sensor for chemical[53,110,6] physical[99], and biological sensors[104,98] detection, drug delivery[39,93,108,69,59] and energy storage[114].

Graphene's optical response changes depending on where it is in the electromagnetic spectrum[81]. Within the visible range, the single-layer graphene sheet is transparent, absorbing 2.3% of the incident light via interband transitions and reflecting less than 0.1% of the transmitted light[73]. Due to the van Hove singularity in graphene, excitonic state generation around 4.6 eV, in which charge carriers are highly associated with binding energy around 0.6 eV, is observable in the high energy ultra-violet range[48]. Despite the fact that graphene can be used as a transparent conductor[100,30] or photodetector[102,14] in light-based device applications, the optical gain within the relaxation process of excited electrons is insufficient in light emission due to the lack of band gap, which directs researchers to investigate ultra thin structures of semiconducting 2D materials and also motivates the discovery of functionalized derivatives of graphene, such as graphane[22,90], graphone[112,45] and fluorographene[83,74].

Apart from unique features of graphene, one of the disadvantages is the absence of band gap. Especially optoelectronic devices need 2D materials with band gap. In 2010, the synthesis of monolayer MoS_2 has created a new excitement in the 2D world after graphene because monolayer MoS_2 is both semiconductor and has a direct band gap which provides luminescence character[91]. After synthesizing MoS_2, its electronic, mechanical and optical properties were investigated for use in new types of technological devices.

Comparing the mechanical properties of graphene and MoS_2, it was determined that graphene is much more durable than MoS_2. Graphene has a strength of 130GPa, while MoS_2 has a strength of 26GPa[78,101]. There is also a big difference between MoS_2 and graphene when comparing electrical conductivity. While the electrical conductivity of graphene is above 1000S/m, despite applying metal addition MoS_2, its electrical conductivity is about 330S/m[105,25]. The discovery of graphene is considered to be revo-

lutionary in materials science. Due to their extraordinary qualities and numerous uses in various branches of science and technology, two-dimensional 2D materials have attracted enormous attention in recent years.

Among these materials, 2D copper iodide has come to be recognized as a very promising option, displaying fascinating properties for applications in optoelectronics[33,29,60], energy storage[68] and catalysis. With its layered arrangement of copper and iodine atoms, 2D copper iodide has a unique crystal structure that makes it possible to build ultrathin, atomically flat sheets with interesting features that set them apart from their bulk counterparts. The electrical and optical characteristics of these atomically thin layers, also known as nanosheets or nanoscale flakes, can be modified by varying their size, thickness, and surface chemistry[89].

Advanced techniques, such as atomic force microscopy AFM[84], scanning electron microscopy SEM[85], can be used to characterize the 2D copper iodide. High-resolution topographic images from an AFM was made it possible to measure the thickness and homogeneity of the nanosheets. The shape, crystal structure, and lattice arrangement of the 2D copper iodide nanosheets were shown by SEM and TEM[107,109]. It was reported that able to evaluate the effectiveness and consistency of the produced nanosheets using these characterization techniques, laying the groundwork for additional property investigation.

Through the use of methods including spectroscopic analysis and electrical transport measurements, the electronic characteristics of 2D copper iodide were examined. To test the charge carrier mobility, conductivity and threshold voltage of the nanosheets, field-effect transistor (FET) devices were made[4]. The vibrational modes and optical characteristics of 2D copper iodide was also studied using spectroscopic methods like Raman spectroscopy and photoluminescence spectroscopy[86,57]. These investigations were provided crucial information for the application of nanosheets in electronic and optoelectronic devices by illuminating their electronic behavior, band structure, and excitonic characteristics[63].

It was investigated the possibilities of 2D copper iodide as a platform for catalysis and energy storage material[67]. The nanosheets are attractive candidates for use in energy storage systems like batteries and supercapacitors due to their distinctive structural features and large surface area. Through the use of galvanostatic charge-discharge tests and cyclic voltammetry, the electrochemical performance of 2D copper iodide was assessed[72]. In order to explore 2D copper iodide's potential as a catalyst, its catalytic activity was also be measured in a variety of reactions, including electrocatalysis and heterogeneous catalysis[24].

Due to their distinct qualities and potential for a wide range of applications, double-

layered honeycomb (DLHC) formations have received a lot of interest lately. A noteworthy example of such a substance is copper iodide CuI from the DLHC which was synthesized in 2021. The structural image of the DLHC CuI is also simulated in the Fig1.1[71]. The utilization of copper iodide in fields like energy storage, ion conduction and electrochemical catalysis is made possible by the enormous interlayer spacing that the DLHC structure of copper iodide offers[94].

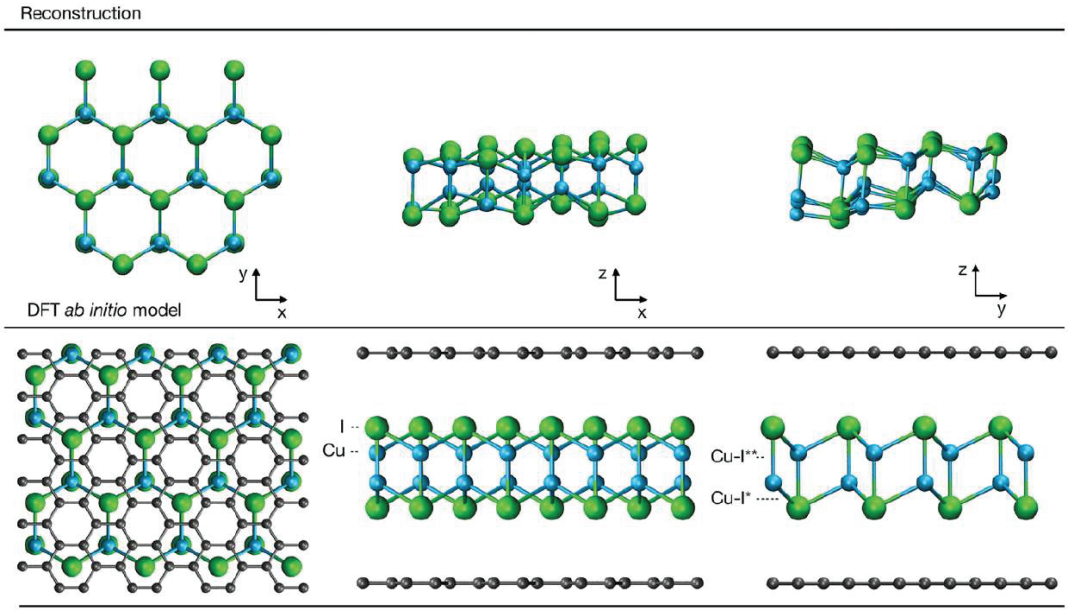

Figure 1.1. Reconstructed 2D h-CuI crystal based on tilt experiments on the top row and an ab initio optimized structure in bilayer graphene encapsulation

Advanced methods such X-ray diffraction XRD, high-resolution transmission electron microscopy HRTEM, and scanning tunneling microscopy STM can used to characterize the structural properties of DLHC copper iodide. The DLHC copper iodide samples' crystal structure, lattice properties, and level of structural disorder can revealed by XRD examination. The visualization of lattice defects and their distribution inside the material can made possible by HRTEM and STM imaging, allowing for a thorough knowledge of the defect-induced structural changes.

In conclusion, the development of DLHC copper iodide, which offers possibilities such as improved light absorption and carrier mobility for nanotechnology. DLHC copper iodide shows significant promise for optical sensing and other technologies.

CHAPTER 2

THEORETICAL BACKGROUND AND METHODOLOGY

Although the macro systems can be defined with Newtonian physics, the much smaller scales have quantum effects. These systems can be described by quantum mechanics using the Schrödinger equation,

$$\hat{H}\Psi(\mathbf{R}_A;\mathbf{r}_i) = E\Psi(\mathbf{R}_A;\mathbf{r}_i) \tag{2.1}$$

where $\hat{H}$ is the Hamiltonian operator, E is the energy eigenvalue of that quantum state. $\Psi(\mathbf{R}_A;\mathbf{r}_i)$ is the wave function. The Hamiltonian is given in Eq. 2.2. The first two terms are the kinetic energies of the nuclei and electrons, respectively, while the third term is the electron-nucleus Coulomb interaction. The fourth term is the electron-electron Coulomb interaction, and finally the last term is the nucleus-nucleus Coulomb interaction.

$$\begin{aligned}\hat{H} = &-\sum_i \frac{\hbar^2}{2m_e}\nabla_i^2 - \sum_A \frac{\hbar^2}{2M_A}\nabla_A^2 - \frac{1}{4\pi\varepsilon_0}\sum_{i,A}\frac{Z_A e^2}{\mid \mathbf{r_i} - \mathbf{R_A} \mid} \\ &+ \frac{1}{2}\sum_{i\neq j}\frac{1}{4\pi\varepsilon_0}\frac{e^2}{\mid \mathbf{r_i} - \mathbf{r_j} \mid} + \frac{1}{2}\sum_{A\neq B}\frac{1}{4\pi\varepsilon_0}\frac{Z_A Z_B e^2}{\mid \mathbf{R_A} - \mathbf{R_B} \mid}\end{aligned} \tag{2.2}$$

The dummy indices i and j are used for electrons and the dummy indices A and B are used for nucleus. The Z_A and Z_B are the nuclear charges. The M_A and M_B are nuclear masses, the $\mathbf{r}$ and $\mathbf{R}$ are spatial coordinates of the corresponding electron and nuclei, respectively. The m_e is the electron mass. The e is the electron charge. The $\hbar$ is the Planck constant, and the $1/4\pi\varepsilon_0$ is the so-called Coulomb constant.

Except for simple systems, such as hydrogen-like systems, or single particles, solving Schrödinger equations when the quantity of interacting particles grows, finding a solution becomes a formidable task. The Schrödinger equation is nearly impossible to solve for systems with plenty of electron-electron interactions. As a result, several methods are employed to approximate the solutions.

The first model that links the energy of a system to its density is the Thomas Fermi model. By considering electrons as a homogeneous electron gas and ignoring their unique movements and interactions, the Thomas-Fermi model, developed in the 1920s, transformed our knowledge of atoms and solids. The Thomas-Fermi methodology offers a computationally efficient way to determine electron concentrations and related properties, offering important insights into the behavior of complicated quantum systems[92]. Despite

having some drawbacks, the Thomas-Fermi model served as a foundation for the creation of more precise quantum mechanical models and is still a key idea in condensed matter physics.

$$T[n] = C_F \int n^{5/3}(r)dr \tag{2.3}$$

where C_F is the Fermi coefficient and n(r) is the electron density. Including electron-nucleus and electron-electron interaction terms makes the total energy of the system;

$$T[n] = C_F \int n^{5/3}(r)dr - Z \int \frac{n(r)}{r}dr + \frac{1}{2}\int\int \frac{n(r_1)n(r_2)dr_1dr_2}{\mid r_1 - r_2 \mid} \tag{2.4}$$

Minimizing the Eq.2.4 gives the ground state energy of the system;

$$N = \int n(r)d^3r \tag{2.5}$$

where n(r) is the electron density.

2.1. Density Functional Theory

Density Functional Theory (DFT) has emerged as a powerful and indispensable tool in the fields of condensed matter physics, materials science, chemistry and biology, due to the fact that some studies in the experimental environment are close to impossible, the conditions are challenging and there is a lot of time loss. Utilizing electron density, DFT saves time for researchers to know the structural, vibrational, optical, electronic and mechanical properties of materials, thanks to its rapid access to results. Since DFT is a versatile tool, it is used very efficiently in the field of nanotechnology and in application studies. With the continuous development of DFT, it has become easier for us to understand materials at the atomic and molecular scale, and has enabled the design of materials with new unique properties.

DFT accurately identifies materials electronic band structure using electron density distribution. It provides information for fundamental properties such as energy levels, binding energies[66], charge transfers[96] between materials and magnetic behaviour[19]. This information is invaluable for understanding and predicting material properties such as catalysis and behaviour of functional materials. DFT deserves great praise for being able to accurately calculate the dynamic stability of materials. Using the computational techniques, researchers can dynamically evaluate materials by examining phonon band structures[5]. This method allows to understand how materials respond to high strength[13]. The ability of DFT to predict these properties has made a great contribution to the field of

materials science, making it possible to discover new materials required for a wide range of applications from the construction industry to energy technology companies.

This section will give a comprehensive overview of density functional theory, covering its foundational ideas, practical uses and significant ideas.

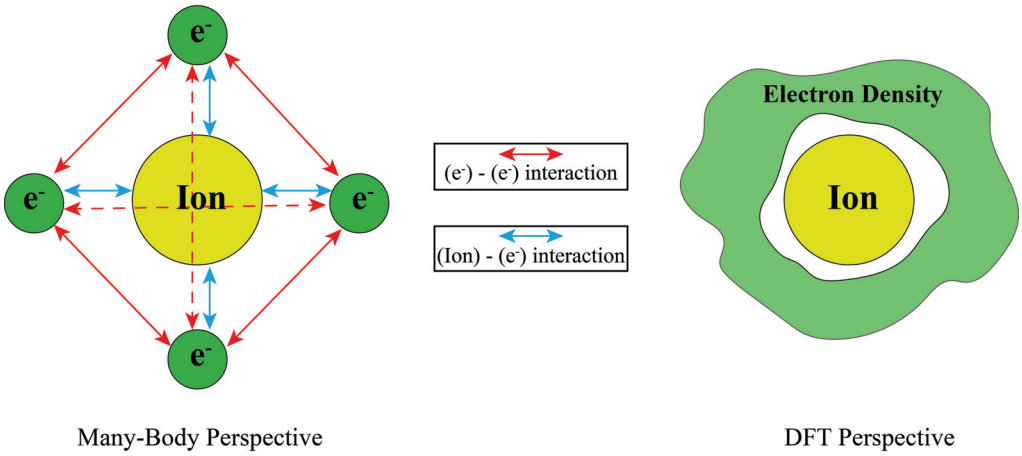

Figure 2.1. DFT approach to a many-body system

2.1.1. Hohenberg-Khon Theorems

Density Functional Theory is based on the Hohenberg-Kohn theorems, which were formulated in 1964 by Pierre Hohenberg and Walter Kohn. These theorems give theoretical basis for the use of DFT in the investigation of the electronic structure and characteristics of atoms, molecules and solids. The fundamental rules governing the relationship between the electron density and the total energy of a system are established by the Hohenberg-Kohn theorems[37]. The ground-state electron density in a many-electron system alone determines the external potential, according to the first Hohenberg-Kohn theorem. In other words, there is a 1:1 relationship between the electron density and the external potential. This suggests that the ground state of the system is completely characterized by electron density. According to the second Hohenberg-Kohn theorem, an electron density's unique function represents the ground-state energy of a system. This theorem implies that the ground-state energy will be equal for two electron concentrations that produce the same external potential.

$$E = < \psi_0 \mid H \mid \psi_0 >= T[n] + V_{int}[n] + E_{II} \int d^3 r V_{ext}(r) n(r)$$
$$T[n] + V_{int}[n] = F_{HK}[n], \tag{2.6}$$

where T[n] is the kinetic energy of electrons, V_{int} is the energy of electron-electron interactions, and E_{II} is the nuclei-nuclei interaction. F_{HK}[n] is a constant which represents to the total kinetic energy of electrons.

2.1.2. Kohn-Sham Equations

According to these theorems, the ground-state energy is a special function of the electron density and the ground-state electron density uniquely determines the external potential. The system is initially generally represented by a collection of non-interacting electrons travelling in an effective potential to solve the Kohn-Sham equations. The exchange-correlation potential, which considers the electron-electron interactions not explicitly considered in the Kohn-Sham equations, is combined with the external potential to form the effective potential.

The Kohn-Sham equations include a group of related self-consistent equations. A single-electron orbital or wave function, referred to as a Kohn-Sham orbital is described by each equation[47]. These orbitals are established by minimizing the total energy functional about the orbital coefficients. To minimize a set of eigenvalue equations must be solved with the eigenvalues standing for the orbital energies. The Kohn-Sham equations are often solved iteratively in practice. Starting with an initial estimation of the electron density, the technique solves the Kohn-Sham equations to generate another set of orbitals.

It is significant to note that the choice of exchange-correlation functional, which approximates the genuine exchange-correlation potential, affects the accuracy of the findings produced from the Kohn-Sham equations. The Kohn-Sham equations offer a useful method for resolving the many-body Schrödinger equation within the context of density functional theory. The Kohn-Sham equations allow for the determination of the electronic structure and characteristics of diverse systems by projecting the interacting electron system onto a system of non-interacting electrons in an effective potential. This equation which allow for the study of complex materials and molecules at the atomic and molecular levels, have shown to be an effective tool in computational materials science, chemistry, and condensed matter physics despite their approximations.

Kohn-Sham method is defined as;

$$E_{KS} = T[n] + \int d^3 r V_{ext}(r) n(r) + E_H[n] + E_{xc}[n] + E_{II}, \tag{2.7}$$

where E_H[n] is called the Hartree energy and given by the following formula,

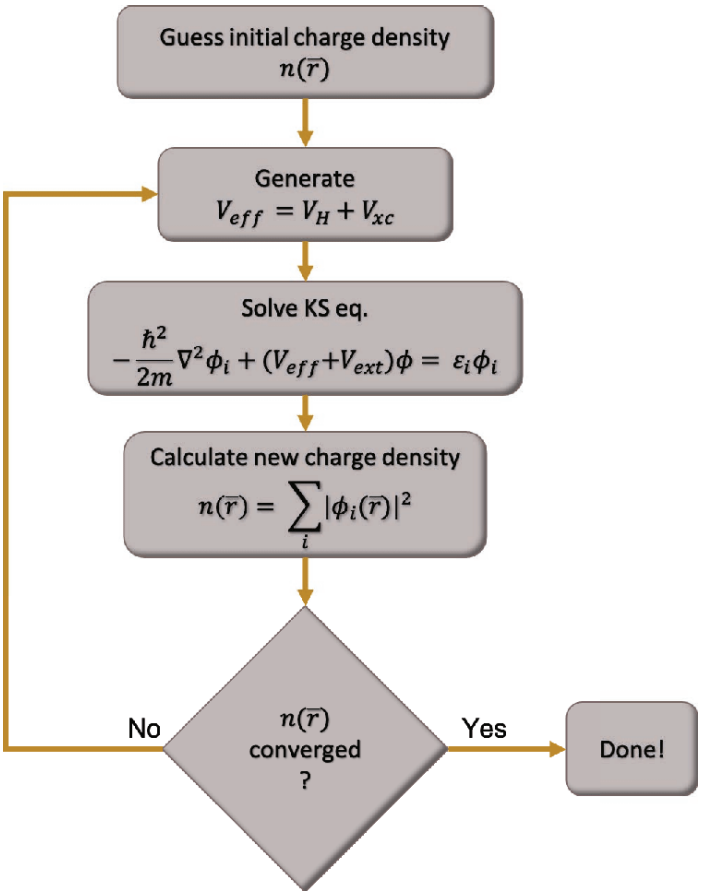

Figure 2.2. Self-Consistent Flowchart

$$E_H[n] = \frac{e^2}{2}\int d^3r d^3r' \frac{n(r)n(r')}{\mid r - r' \mid}. \tag{2.8}$$

The Schrödinger like equation of non-interacting electrons is,

$$\hat{H}_{KS}\psi_i(r) = \varepsilon_i\psi_i(r), \tag{2.9}$$

where H_{KS} and ε_i are effective Kohn-Sham Hamiltonian and energy eigenvalues, respectively. ψ_i(r) are the single-particle wave functions or Kohn-Sham orbitals. Spin operators are not taken into account to simplify the equation. Kohn-Sham orbitals and ground-state electron density functional relation is given by,

$$n(r) = \sum_{i=1}^{N} \mid \psi_i \mid^2, \tag{2.10}$$

and the effective Hamiltonian is,

$$\hat{H}_{KS}(r) = -\frac{1}{2}\nabla^2 + V_{KS}(r), \tag{2.11}$$

in which the effective Kohn-Sham effective potential, V_{KS}(r),

$$V_{KS}(r) = V_{ext}(r) + V_H(r) + V_{xc}(r), \tag{2.12}$$

that is the total of the external, V_{ext}(r) Hartree, V_H(r) and exchange-correlation, V_{xc}(r) potentials, respectively.

In many scientific disciplines, especially quantum mechanics and computational physics, the self-consistent approach is a essential method. This effective strategy entails working through a series of equations until a reliable solution is found. The self-consistent method captures the interdependence of variables and enables a more accurate description of complex systems by adding feedback between the solution and the problem itself as seen in Fig2.2[41]. Through this iterative process, the solution is gradually improved and eventually converges to a self-consistent solution that satisfies all constraints and equations. The self-consistent method has found widespread use in a variety of fields, including modeling of fluid dynamics and electromagnetism as well as calculations of electronic structure in materials science and quantum chemistry. The self-consistent approach has developed into a crucial instrument for researching and comprehending complicated phenomena in the natural sciences due to its capacity to control intricate interactions and maximize solutions.

2.1.2.1. Exchange-Correlation Functionals

In Density Functional Theory, exchange-correlation functionals play a significant role in order to examine the electronic structure of atoms, molecules and solids by using computational techniques[47,79]. In a system with many electrons, the exchange and correlation effects that result from these interactions are roughly represented by these functionals. Therefore using the correct approximation of exchange correlation energy for a material is of importance.

Local Densiy Approximation (LDA): According to the local density approximation, the system has been divide into volumes with constant electron densities[15].

$$E_{xc}^{LDA}[n] = \int n(r)\varepsilon_{xc}^{hom}[n(r)]d^3r \tag{2.13}$$

where ε_{xc}^{hom} is the exchange-correlation energy density of homogeneous electron gas of an electron density, n(r). LDA functional is effective in systems like metals where the

electron density fluctuates gradually. However, cohesive energies are typically overstated while lattice dimensions are typically underestimated.

Generalized Gradient Approximation (GGA): The electron concentrations in the generalized gradient approximation do not remain constant between divisions but rather change with a gradient[80].

$$E_{xc}^{GGA}[n] = \int f^{GGA}(n(r), \nabla n(r)) d^3r \tag{2.14}$$

where possible electron density, n(r), the gradient of the electron density, $\nabla n(r)$. GGA functions effectively with systems that have rapidly fluctuating electron densities, in contrast to LDA.

2.1.3. Hellman-Feynman Theorem

The Hellmann-Feynman theorem is named after Henry C. Hellmann and Richard P. Feynman who independently formulated the theorem, it establishes a connection between the derivative of the total energy of a system with respect to an external parameter and the expectation value of the derivative of the Hamiltonian.

The computing efficiency of the Hellman-Feynman theorem is one of its main advantages. The theorem provides the determination of the derivative of the energy directly from the eigenstates and eigenvalues of the Hamiltonian, avoiding the need to solve the Schrödinger equation for various parameter values. Additionally, the Hellmann-Feynman theorem establishes a relation between the energy and the forces associated with the system[34]. The theorem connects the derivative of the energy with respect to the particle's position to the inverse of the force applied by taking the parameter to be the particle's position. Through this relation , it is possible to calculate forces, examine potential energy surfaces and run molecular dynamics simulations.

$$\frac{\partial E}{\partial \lambda} = \langle \frac{\partial \hat{H}}{\partial \lambda} \rangle \tag{2.15}$$

where $\frac{\partial E}{\partial \lambda}$ is the derivative of the total energy E with respect to an external parameter λ, $\langle \frac{\partial \hat{H}}{\partial \lambda} \rangle$ is the expectation value of the derivative of the Hamiltonian $\hat{H}$ with respect to the same parameter λ.

2.1.4. Hybrid Functionals

Electronic band structures of materials can be estimated with DFT calculations by using LDA and GGA approaches, but the experimentally observed electronic bandgap may not be perfectly approximated. By using hybrid functions it is possible to bypass the disadvantages of standard exchange-correlation functionals. These functionals are appropriate for a variety of systems because they provide a balanced performing of exchange and correlation effects. B3LYP[11,55,12], PBE0[2,23], and HSE06[36,35,52] are a few examples of hybrid functionals. Exchange-correlation energy by HSE;

$$E_{xc}^{HSE} = aE_x^{HF,SR}(\omega) + (1-a)E_x^{PBE,SR}(\omega) + E_x^{PBE,LR}(\omega) + E_c^{PBE} \tag{2.16}$$

where $E_x^{HF,SR}$ corresponds to the contribution from short-range HF exchange, $E_x^{PBE,SR}$ and $E_x^{PBE,LR}$ refers to short- and long-range parts of the PBE exchange energy, and E_c is the PBE correlation energy.

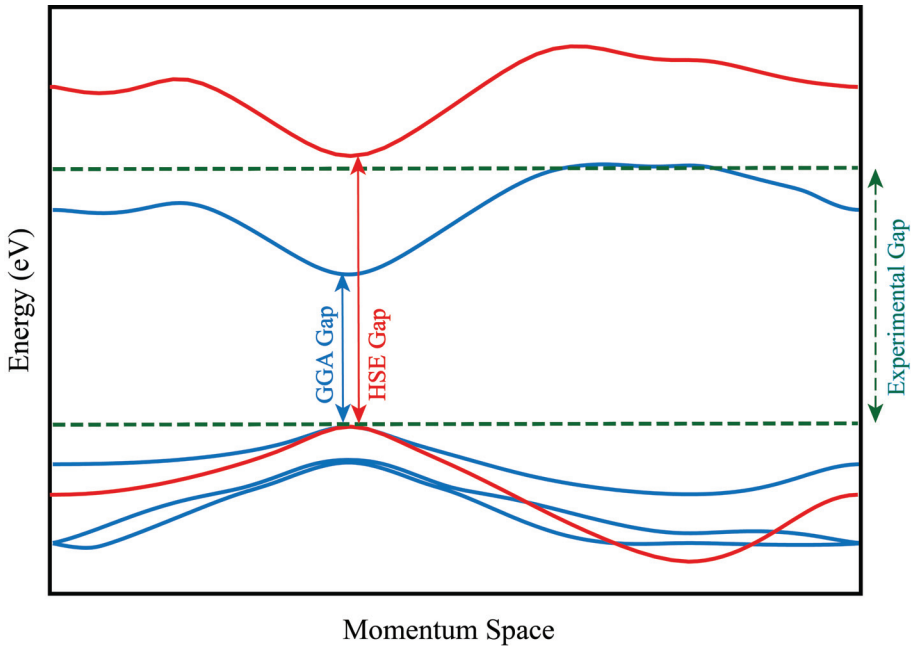

Figure 2.3. Schematic of HSE and GGA approaches according to the experimental result

2.2. Computing Phonons

Lattice vibration's quantum mechanical description is referred to as a "phonon" in this context. A material's vibrational characteristics is plotted as its phonon band dispersion via the Brillouin zone. Atomic displacements will produce forces that return the system to equilibrium, much like in a simple spring and these oscillations will follow Hooke's law;

$$F = -kx \tag{2.17}$$

where *k* is the spring constant, and *x* is the distance between atom and equilibrium position. In this section, methodology of phonon band dispersion calculations in DFT is discussed.

In density functional theory, computations are performed at absolute zero temperature (0 K), which means that the solution does not inherently include information about vibrations. Nonetheless, as mentioned earlier, when an atom is displaced from its equilibrium position, a restoring force is generated and this force can be calculated. This approach is commonly known as the small displacement method. The force constant matrix is obtained by perturbing the position of an atom by a small amount within a suitably large supercell. The number of atoms to be displaced depends on the system's symmetry. For each displacement, the Hellman-Feynman forces are calculated, and a force matrix is constructed. At low temperatures, the potential energy of a crystal can be expressed using the following equation:

$$U_{harm} = E_{eq} + \frac{1}{2} \sum_{ls\alpha, l't\beta} \phi_{ls\alpha, l't\beta} \upsilon_{ls\alpha} \upsilon_{l't\beta} \tag{2.18}$$

where E_{eq} is the total energy of the crystal at equilibrium positions, υ_{ls} is the displacement of atom s in unit cell *l*, α, and β denotes the direction of the displacement in cartesian coordinates, $\phi_{ls\alpha, l't\beta}$ is the force constant matrix. Differentiation of the harmonic energy in Eq. 2.18 relation between the forces and the displacements can be deduced. The relation is linear, as $F_{ls\alpha}$ is found to be;

$$F_{ls\alpha} = -\sum_{l't\beta} \phi_{ls\alpha, l't\beta} \upsilon_{l't\beta} \tag{2.19}$$

After solving the dynamical matrix, it is to compute the eigenvalues, which correspond to the phonon frequencies for each phonon branch. The total number of phonon branches can be determined by considering the total number of degrees of freedom in the crystal, which is 3N for a system composed of N atoms in the primitive cell. Among these branches, 3 are classified as acoustical, while (3N-3) are considered optical. Acoustical

branches represent in-phase atomic motions, while optical branches depict out-of-phase motions of the atoms. The vibrational characteristics were calculated using the PHON[50,5] and PHONOPY algorithm[51,49].

2.3. Computational Parameters

In this thesis, structural optimizations and electronic band dispersions were studied using first-principles calculations within the density functional theory, employing the Vienna Ab initio Simulation Package[51,49]. The Perdew-Burke Ernzerhof (PBE) variant of the generalized gradient approximation (GGA) was utilized to approximate the exchange-correlation potential. Additionally, the plane-wave projector-augmented wave potentials were employed.

In calculation performed here, the energy cutoff value was set at 500 eV, the kinetic energy cutoff at 10^{-5} eV. The DFT-D3 approach of Becke-Johnson was used to approximate the van der Waals (vdW) interaction[32]. The Bader method was used to determine the transfer of charge between atoms. Vacuum separation of 15 Å was chosen along the z-axis to prevent interactions with neighboring cells. A $12 \times 12 \times 1$ k-point mesh was used for the structural optimization of the basic unit cell, and it was doubled for calculations involving the density of states to ensure greater accuracy. The Heyd-Scuseria Ernzerhof (HSE06) functional was used to calculate better assumptions of electrical properties because GGA understates the band gap. The cohesive energy per atom was obtained with the given formula;

$$E_{coh} = \frac{n_{Cu}E_{Cu} + n_I E_I - E_{sys}}{n_{tot}} \tag{2.20}$$

where n_{Cu} and n_I are number of atoms per unitcell for Cu and I respectively. Single atom energies for Cu and I atom are provided by E_{Cu} and E_I, respectively. n_{tot} refers to the total number of atoms in a unit cell. For the calculation of Raman spectra, the zone centered vibrational modes were calculated using small-displacement methodology. The corresponding Raman activity of each phonon mode was obtained through the derivative of the macroscopic dielectric tensor using the finite-difference method. Also strain calculations were performed as biaxial and uniaxial direction.

2.4. Mechanical Properties of Materials

The mechanical properties of a material are related to the physical properties of that material under external forces. Materials can be subjected to strain or deformation, especially in the experimental environment. Thanks to the mechanical properties, it can be understood how the materials will react to such external influences. Some of the important mechanical properties are durability, hardness, ductility, toughness, tiredness resistance. Durability is the strength of a material to withstand permanent deformation under an applied external force. The resistance of a material to scratching is called hardness. The ability of a material to undergo plastic deformation without fracture is called ductility. Toughness is related to the energy absorption capacity of a material before it fractures. Studying the mechanical properties of materials is important for the aerospace, automotive and construction industries.

2.4.1. Elastic Constants

Elastic constants are physical parameters related to the elastic behaviour of materials. These constants are calculated by examining the relationship between the stress applied to a material and the resulting strain. Young's modulus (E), shear modulus (G) and Poisson's ratio are examples of the most fundamental elastic constants. Young's modulus is related to the stiffness of a material in the axial direction and expresses the ratio of stress to strain along the axis. Shear modulus is the ratio of shear stress to shear strain and measures the resistance to shear deformation. Poisson ratio expresses the ratio of lateral strain to longitudinal strain. It gives information about the shrinkage and expansion properties of the material according to the applied stress. The determination of elastic constants for materials that require reliable elastic behavior is particularly important in the engineering field.

2.4.1.1. Young Modulus

Young's modulus which is measuring the hardness of a material is an essential mechanical property. Young's modulus, also called elastic modulus or modulus of elasticity.

This concept was first introduced by Thomas Young and named after this scientist. Young's modulus measures the ratio of stress to strain under tensile and compressive strain.

Mathematically, Young's modulus (E) is calculated by dividing the stress (σ) applied to a material by the resulting strain (ε):

$$E = \frac{\sigma}{\varepsilon} \tag{2.21}$$

Young's modulus is expressed in units of pressure, such as pascals (GPa). In the elastic deformation region, the slope of the stress-strain curve is related to Young's modulus. For example, steel has a high Young's modulus and is highly resistant to deformation. But if we consider the same situation for rubber material, it has low Young's modulus and shows high flexibility.

2.4.1.2. Poisson Ratio

The Poisson's ratio is a dimensionless parameter that quantifies the lateral contraction or expansion of a material that is subjected to axial stress. This concept was first named by French mathematician and physicist Simeon Poisson at the beginning of the 19^{th} century.

Poisson's ratio (ν) is defined as the negative ratio of the transverse or lateral strain ($\varepsilon_{lateral}$) to the axial or longitudinal strain (ε_{axial}):

$$\nu = \frac{\varepsilon_{lateral}}{\varepsilon_{axial}} \tag{2.22}$$

If Poisson ratio value is between 0 and 0.5 indicates when material has axial tensile strain, it shrink laterally but when material has compressive strain, it expands laterally expands. On the other hand, a negative Poisson's ratio between -1 and 0 is observed in a few special materials known as auxetic materials, which expand laterally under tension and shrink laterally under compression. The atomic or molecular structures of the materials determine the Poisson ratios. For example, metals have a very regular structure so Poisson ratios are around 0.3. Polymers have an irregular structure so Poisson ratios are close to 0.5. Also, materials with a higher Poisson ratio are more ductile, while materials with a lower ratio are more brittle.

2.4.2. Elastic Constants in 2D Limit

Two important elastic constants such as Young's modulus and Poisson's ratio were mentioned in previous sections, but these elastic constants need to be redefined if a 2D material is to be analysed. This section discusses how to use these two elastic constants for 2D materials.

2.4.2.1. In-plane Stiffness

When the modulus of elasticity is considered for the 2D limit, it is called in-plane stiffness. Since there are no periodic boundaries in the out-of-plane direction in 2D materials, in-plane stiffness must be related to in-plane stress and strain. Therefore, the equation in 2.21 should be redefined as:

$$C_{xx} = \frac{\sigma_{xx}}{\varepsilon_{xx}} \tag{2.23}$$

where the directions xx and yy indicate special directions in the 2D crystal structure. If we think for a hexagonal structure, these directions refer to ZZ and AC directions. In-plane stiffness value is the same for each direction in the isotropic materials. The reason is that the interatomic bonding symmetry of the crystal structure. But if we consider the same situation for anisotropic materials, there are different in-plane stiffness values in different directions. The fact that the resistance of the material is not the same in all directions is an advantage for nanotechnology applications.

In atomic limit dimensions, in-plane stiffness is calculated depending on the relationship between applied strain and strain energy. Strain energy is the change in the total energy of a material due to applied strain. these elastic constants are calculated in the linear elastic region, the strain energy formula is as follows :

$$E_S = c_1\varepsilon_{xx}^2 + c_2\varepsilon_{yy}^2 + c_3\varepsilon_{xy}^2 \tag{2.24}$$

where E_S is the strain energy, defined by the relationship between the energy of the relaxed structure and the energy of the strained structure. The coefficient c_i are calculated by the formula :

$$C_x = \frac{1}{A_0}\left(2c_2 - \frac{c_3^2}{2c_1}\right) \tag{2.25}$$

$$C_y = \frac{1}{A_0}\left(2c_1 - \frac{c_3^2}{2c_2}\right) \tag{2.26}$$

where A_0 is the strain free area in the structure.

It is possible to calculate in-plane stiffness with the elastic parameters calculated using the elastic tensor. Elasticity tensor has a dimension of 6x6 as seen in the form ;

$$\begin{bmatrix} C_{1111} & C_{1122} & C_{1133} & C_{1123} & C_{1131} & C_{1112} \\ C_{2211} & C_{2222} & C_{2233} & C_{2223} & C_{2231} & C_{2212} \\ C_{3311} & C_{3322} & C_{3333} & C_{3323} & C_{3331} & C_{3312} \\ C_{2311} & C_{2322} & C_{2333} & C_{2323} & C_{2331} & C_{2312} \\ C_{3111} & C_{3122} & C_{3133} & C_{3123} & C_{3131} & C_{3112} \\ C_{1211} & C_{1222} & C_{1233} & C_{1223} & C_{1231} & C_{1212} \end{bmatrix}$$

where C_{ijkl} is the elastic constants have some symmetry properties such as ;

$C_{ijkl} = C_{jikl}$, $C_{ijkl} = C_{ijlk}$, $C_{ijkl} = C_{klij}$. The number of independent constants reduces to 21 for this reason. At the same time this number is the maximum number of independent elements.This number can vary from 3 to 21 depending on the symmetry of the material.

The elasticity tensor form for isotropic materials is ;

$$\begin{bmatrix} C_{11} & C_{12} & C_{12} & 0 & 0 & 0 \\ C_{12} & C_{11} & C_{12} & 0 & 0 & 0 \\ C_{12} & C_{12} & C_{11} & 0 & 0 & 0 \\ 0 & 0 & 0 & C_{33} & 0 & 0 \\ 0 & 0 & 0 & 0 & C_{33} & 0 \\ 0 & 0 & 0 & 0 & 0 & C_{33} \end{bmatrix}$$

where C_{33} is calculated with C_{11} and C_{12} by the relation ;

$$C_{33} = \frac{C_{11} - C_{12}}{2} \tag{2.27}$$

$$C_{11} = \frac{E(1-v)}{(1+v)(1-2v)} \tag{2.28}$$

$$C_{12} = \frac{Ev}{(1+v)(1-2v)} \tag{2.29}$$

E is the modulus of the elasticity and ν is the Poisson ratio. E, which is the modulus of elasticity used for 3-dimensional structures, can be correlated with the in-plane stiffness by using the effective thickness of the 2D structure. The effective thickness,h_e is calculated

by adding the layer thickness of the material and the interlayer space. Then C and E are related by the formula ;

$$C = Eh_e \tag{2.30}$$

By using the equation 2.28, 2.29 and 2.30, C can rewrite in terms of elastic constants as ;

$$C = h_e C_{11}[1 - \left(\frac{C_{11}}{C_{12}}\right)^2] \tag{2.31}$$

This elastic tensor can be calculated directly by DFT. It is also possible to calculate Poisson ratio using elastic tensor as seen follow equation ;

$$v = \frac{C_{12}}{C_{11}} \tag{2.32}$$

It has been mentioned so far about elastic mechanical constants and how to calculate Poisson ratio and in-plane stiffnes by using DFT calculations. In the next section, other mechanical parameters such as ultimate strength are mentioned, using the strain-stress relationship.

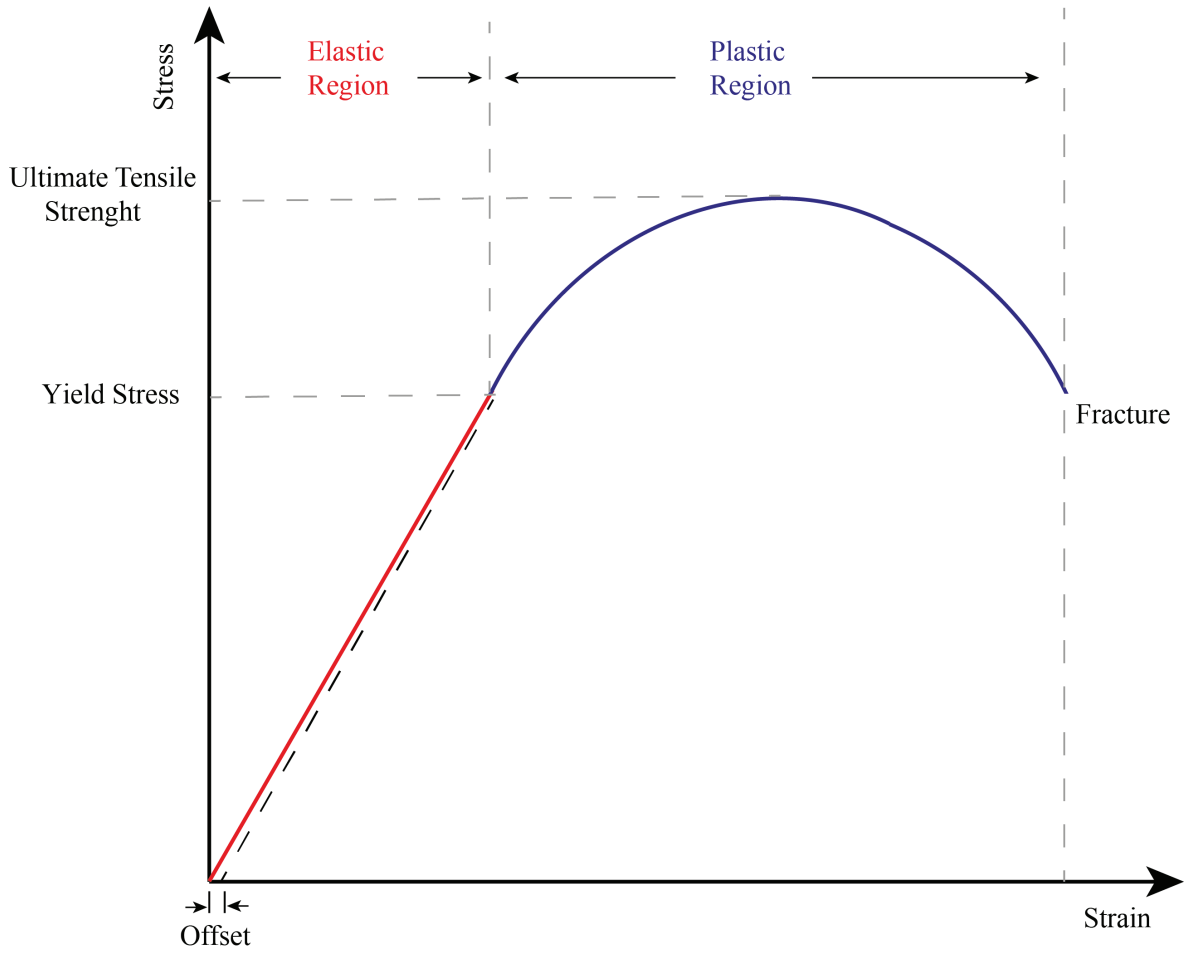

Figure 2.4. A general strain-stress curve demonstrating elastic and plastic regions

CHAPTER 3

FIRST PRINCIPLE INVESTIGATION OF 2D CuI CRYSTAL

Followed by the successful synthesis of ultra-thin form of C atoms, namely graphene, in 2004[28,77], two-dimensional (2D) materials have become the potential candidates for the applications in nanotechnology. Apart from the various types of 2D materials synthesized up to date, recent experiments demonstrated the synthesis of ultra-thin materials in the form of double layer hexagonal crystal (DLHC), such as single-layers of MnSe[1], AlSb[82], and CuI[71]. Among the DLHC single-layer structures, CuI was reported to be stable when sandviched between graphene oxide layers at low temperatures, although its layered bulk form was known to occur at elevated temperatures between 645 K and 675 K[71].

Bulk copper iodide refers to a solid compound composed of copper and iodine atoms, existing in a crystalline form. When copper salts interact with iodide ions in aqueous solutions, it results in the formation of bulk copper iodide. This compound exists as a crystalline solid and can adopt different crystal structures, including zincblend-CuI, wurtzite-CuI, and cubic-CuI[38]. Bulk copper iodide has a high ionic conductivity, which is one of its most remarkable properties and makes it a possible candidate for use as an electrolyte in batteries and other electrochemical devices[95]. The maximum hole conductivity for optically transparent p-type semiconductors was observed in the zinc blende Γ phase of copper iodide[31]. Additionally, studies have shown that its low thermal conductivity is advantageous for thermoelectric applications because it enables effective heat to electricity conversion[103]. Due to its high electromagnetic spectrum absorption coefficient in the visible range, bulk copper iodide has recently attracted increasing interest for usage in photovoltaic components like solar cells[16]. Bulk copper iodide has also been researched as a potential component for LEDs since it possesses satisfying luminous[113]. Since 2D copper iodide has unusual physical and chemical characteristics, it has been the subject of extensive research. The distinctive electrical characteristics of 2D copper iodide are one of its main advantages. Furthermore, the 2D copper iodide has high carrier mobility, enabling fast and low-resistance movement of electrons and holes. This makes it a suitable material for high-speed transistors, essential for electronic devices.[17]. The use of 2D copper iodide in catalysis is another potential use. The substance is an excellent catalyst for many different processes such as improving CO adsorption on Cu because of

its huge surface area and high surface energy[56]. The CuI crystal, which was synthesized recently in the 2D DLHC phase has an in-plane bond as well as an out-of-plane bond structure[71]. Additionally, DLHC-CuI is a promising candidate for use in nanoelectronics and nanomechanics due to its excellent mechanical properties and ease of synthesis.

Changes in the strain of a material can lead to changes in the electronic or structural state of that material. It was investigated single-layer MoS_2 photodetectors that are transparent and flexible under the influence of biaxial strain[26]. In another study, it was explored the intercoupling between strain and magnetic property as it relates to half-fluorinated single layers of BN, GaN, and graphene. For half-fluorinated BN, GaN, and graphene sheets, first-principles calculations show that the energy difference between ferromagnetic and antiferromagnetic couplings strongly rises with strain[62]. Until now, halogens have been used many times in semiconductor technology, but they are less common than other semiconductors. The strain-related changes in the electronic and structural properties of CuI, which is a halometal, especially in the 2D-DLHC phase have been wondered and this subject has been examined in this article.

In the present work, the structural, electronic, vibrational, and mechanical properties of single-layer DLHC form of CuI were investigated by means of first-principles calculations. The paper was organized as follows; the results for the structural Sec. 3.1, vibrational Sec. 3.2, and the electronic properties Sec. 3.3 of single-layer CuI are discussed. The Sec. 3.4 is devoted to the strain properties of single-layer CuI exposed to external uniaxial strain. Finally, the Sec. 3.5 includes our conclusions.

3.1. Structural Properties

The top and side views of the crystal structure of single-layer CuI is shown in Fig. 3.1(a). The single-layer of CuI consists of two Cu layers sandviched between the upper and lower I layers. The optimized crystal structure reveals the two in-plane lattice parameters to be equal to each other, a=b=4.08 Å, as a result of the in-plane isotropy of the structure. The Cu-I bond lengths are calculated for the two directions such as in-plane (d_{ip}) and out-of-plane (d_{op}), which are found to be 2.59 and 2.67 Å, respectively. The thickness of single-layer CuI, which is defined as the distance between the outer most atoms in the lattice, is calculated to be 3.85 Å. As compared to the structural parameters of DLHC structure of the experimentally realized AlSb (a=b=4.24 Å)[8], CuI exhibits a smaller lattice as a result of smaller atomic radii of Cu and I atoms as compared to those for Al and Sb.

Table 3.1. For the single-layer of CuI and bulk CuI; optimized in-plane lattice parameters, a, b, c; the bond length between Cu and I along the in-plane and out-of-plane directions, d_{ip}^{Cu-I} and d_{op}^{Cu-I}; the amount of charge donated by a Cu to I atoms, ρ_{Cu-I}; calculated cohesive energy per atom, E_{coh}; the work function, ϕ; electronic band gap energy, E_{gap}.

	a (Å)	b (Å)	c (Å)	d_{ip}^{Cu-I} (Å)	d_{op}^{Cu-I} (Å)	ρ_{Cu-I} e	ϕ (eV)	E_{coh} (eV/atom)	E_{gap} eV
DLHC-CuI	4.08	4.08	-	2.59	2.67	0.3	4.50	3.05	1.83
Bulk-CuI(Zincblende)	4.22	8.45	7.31	2.58	2.59	0.3	2.19	3.16	1.29
Bulk-CuI(Wurtzite)	4.21	4.21	6.95	2.58	2.59	0.3	2.72	3.16	1.34

The cohesive energy of single-layer CuI, which is calculated using the Eq.2, is found to be 3.05 eV/atom which is lower as compared those of well-known single-layer materials such as graphene has 7.74 eV[21] and MoS_2 has 4.98 eV[3]. Moreover, according to Bader charge analysis when single-layer CuI is formed, each Cu atom donates 0.3 e while each I atom receives 0.3 e. The work function of the CuI layer is also calculated using the formula, $\Phi = E_V - E_F$, where E_V is the vacuum energy, in which electrons are supposed to behave as free-electrons, and E_F is the Fermi energy. The work function is found to be 4.50 eV which is lower than those of graphene (4.60 eV)[111] and MoS_2 (5.15 eV)[18].

3.2. Vibrational Properties

The dynamical stability of single-layer CuI is investigated by performing phonon band dispersion calculations thorught the BZ and the obtained result is presented in the Fig. 3.1(b). It appaers from the phonon dispersions that single-layer CuI is dynamically stable as a free-standing layer as revealed by the non-imaginary phonon frequencies. Apart from the three acoustical phonons, there exists nine optical phonon branches three of which are non-degenerate. In order to investigate the dynamical properties of single-layer CuI in detail, first-order off-resonant Raman spectrum is calculated and four Raman active phonon modes are shown in the Fig. 3.1(c). The lowest frequency Raman active phonon mode is calculated to be at 37 cm^{-1} which is a doubly-degenerate vibration along the in-plane directions. It stems from the out-of-phase vibration of top and bottom Cu-I pairs. The two of the three Raman active modes are found to be non-degenerate and are found to be at frequencies 107 and 152 cm^{-1}, respectively. The phonon mode having frequency 107 cm^{-1} arises from the out-of-phase vibration of Cu and I atoms residing at either top or

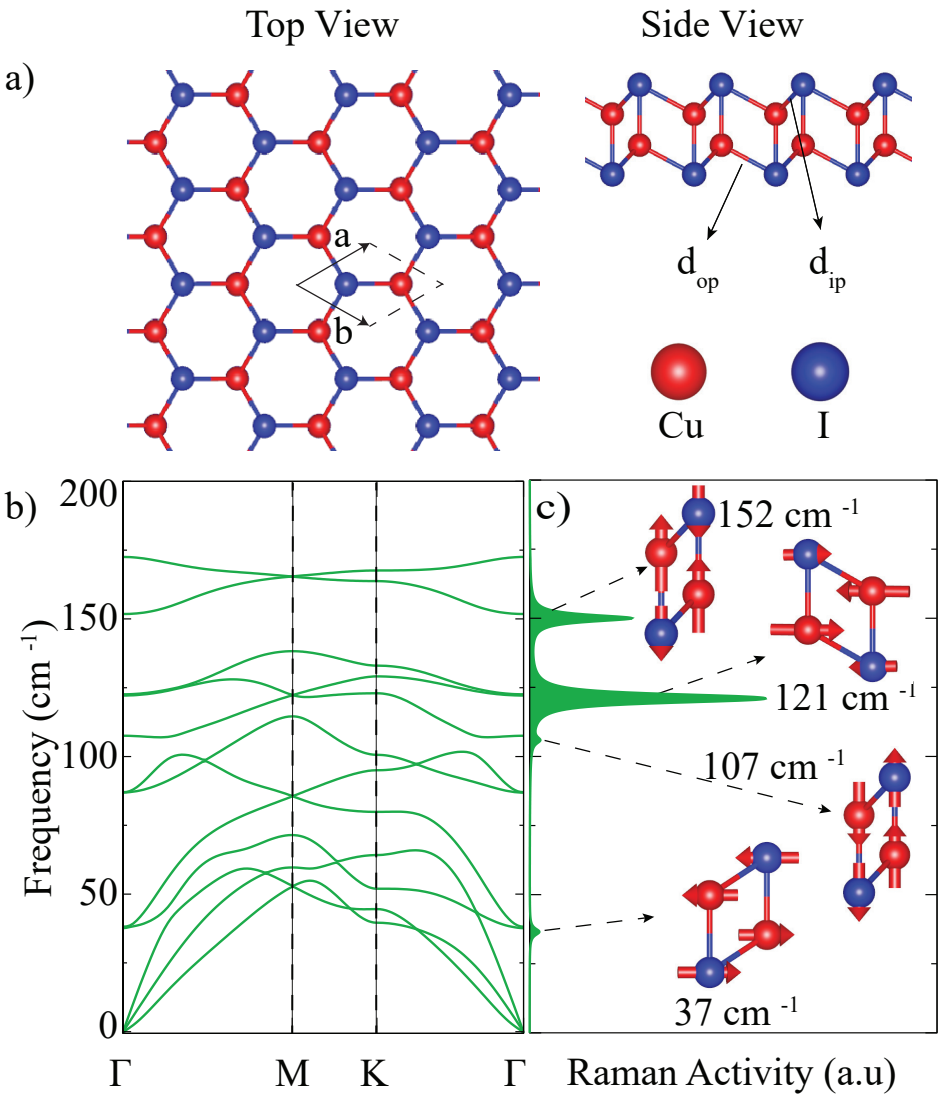

Figure 3.1. (a)Top and side view ML-DLHC CuI.(b)Phonon band structure of CuI.(c)Raman spectrum of ML-DLHC CuI and Phonon forces of ML-CuI

bottom layer along the out-of-plane direction. Similarly, the phonon mode at 152 cm^{-1} has an out-of-plane vibrational characteristic in which the top and bottom Cu-I pairs vibrate out-of-phase with respect to each other while the Cu and I atoms at the same plane also vibrate oppositely. The another doubly-degenerate phonon mode is calculated to have a frequency of 121 cm^{-1} and it stems from the opposite vibration of top and bottom Cu-I pairs along the in-plane directions.

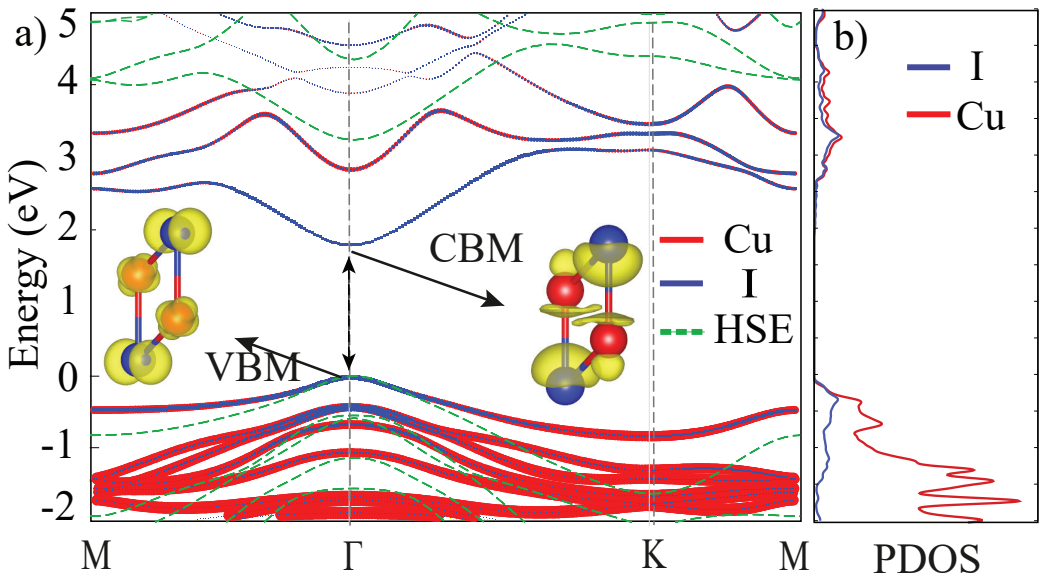

Figure 3.2. (a)Electronic band structure of CuI, HSE band structure and Partial DOS graph of CuI. (b)Conduction band minimum (CBM) and the valence band maximum (VBM) at the Γ point

3.3. Electronic Properties

The electronic properties of single-layer CuI are investigated by means of its electronic bands and the corresponding partial density of states (PDOS). As shown in Fig. 3.2(a), single-layer CuI exhibits a direct band gap semiconducting behavior with an electronic band gap of 3.24 eV. The valence band maximum (VBM) and the conduction band minimum (CBM) are found to reside at the Γ point of the BZ. The insets show the atomic orbitals dominating and contributing to the VBM and CBM states. Apparently, the VBM state is dominated by the p_x and p_y orbitals of I atom while relatively less contribution of Cu-d orbitals are calculated. The CBM state is shown to be dominated by the I-s orbitals with a tiny contribution from the Cu-p_z orbitals. In addition, the effective masses of the charge carriers corresponding to the VBM and CBM states are calculated and the results are listed in Table I. The electron and the hole effective masses are calculated to be 0.53 and 0.66 m_0, respectively which are comparable to those calculated for single-layer MoS_2 (0.54 and 0.44 m_0 for the electrons and holes, respectively)[43].

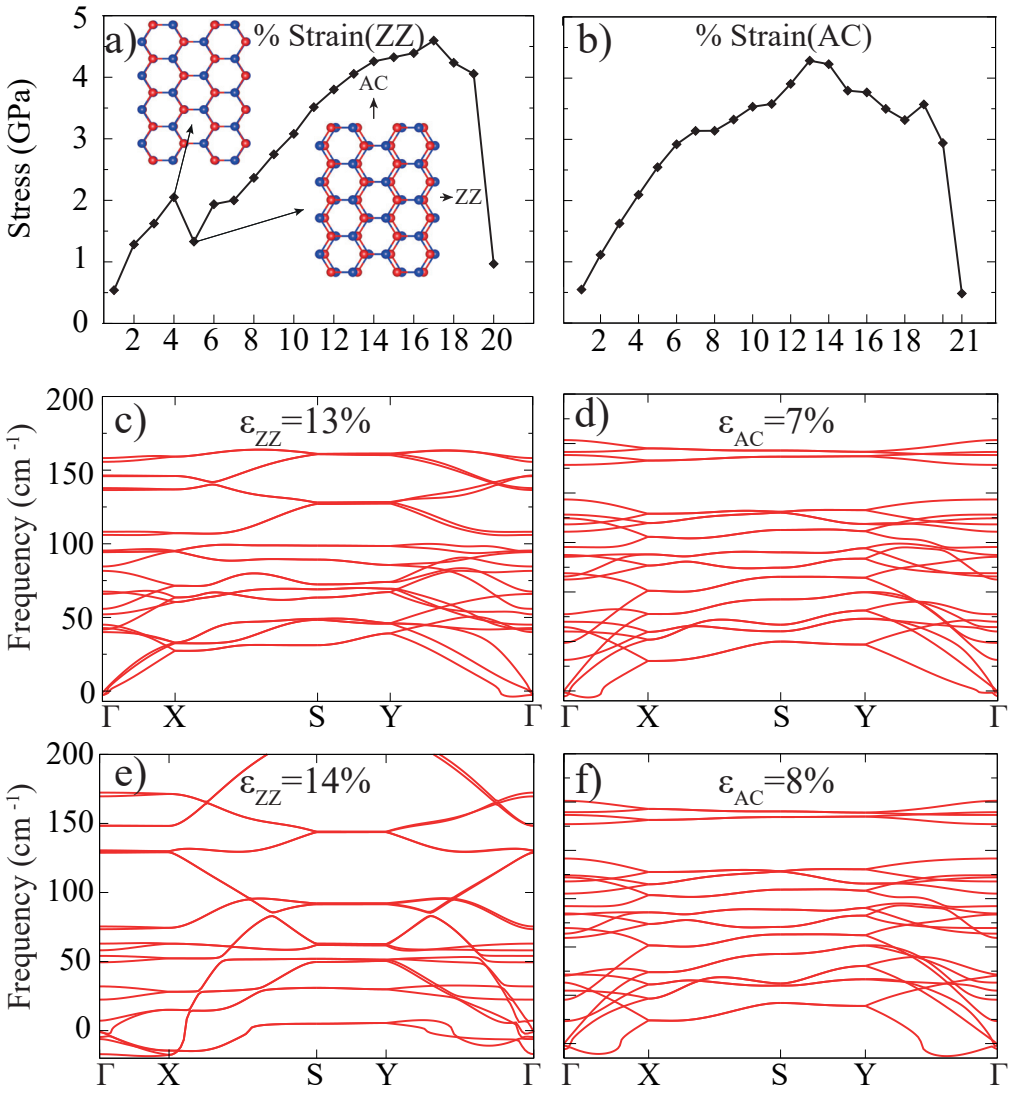

Figure 3.3. Strain–Stress graph by uniaxial directions and phononic stability of primitive cell CuI.

3.4. Strain-dependent properties

Strain changes the electronic properties of the material in experimental or theoretical calculations. That's why strain tests are very important, especially for 2D materials. The change in the electronic band structure of CuI depending on the biaxial strain between %-5 and %+5 is shown in Fig.3.4(a) in the calculation of biaxial strain from %-5 compressive to %5 tensile, the change in electronic band structure was calculated for the hexagonal primitive cell. In the strain calculation applied from %-5 compressive to %5 tensile for the hexagonal CuI primitive cell, it is seen that the VBM band edge does not change

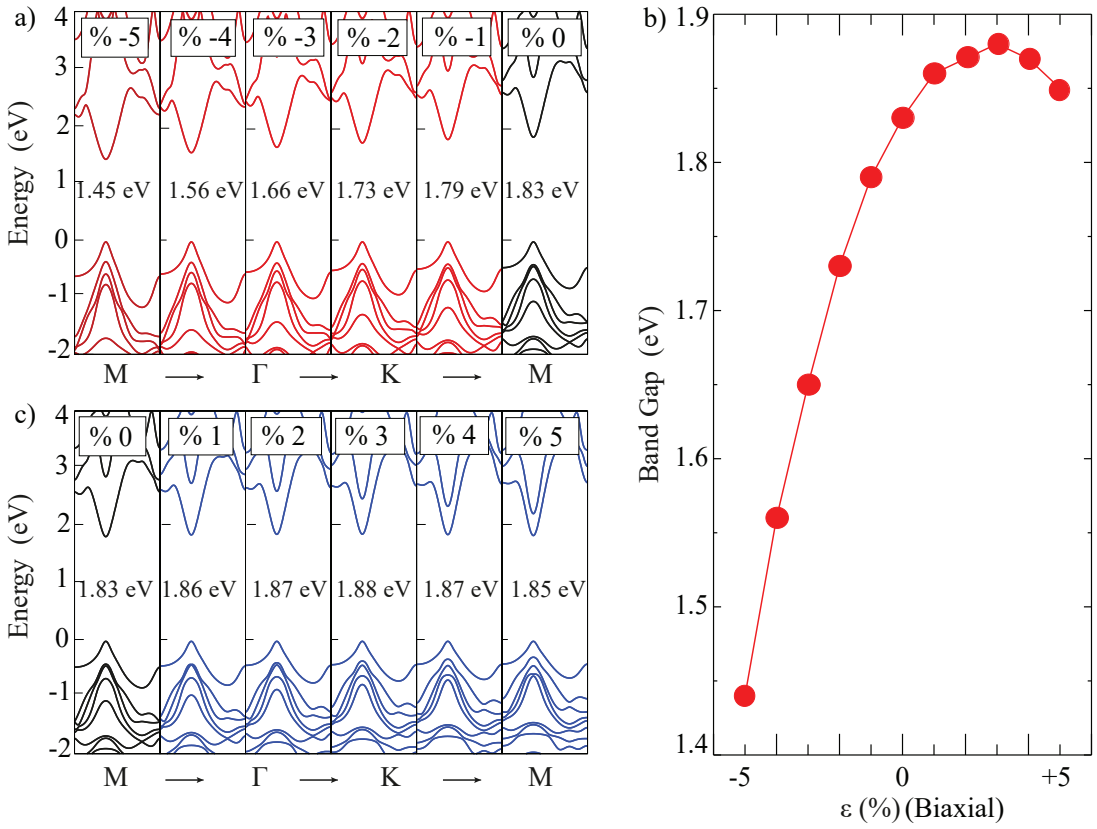

Figure 3.4. Biaxial Strain dependent on the electronic band structure of DLHC CuI.

much. In addition, when increasing strain, it is understood that the second dispersion of the conduction band, approaches to the conduction band minimum point. Also in the Fig.3.4(b), the band gap increase is shown graphically. While a rapid increase was found from %-5 strain to the unstrained state, the increase towards %5 tensile strain decreased. Even %3 strain reached saturation point. A rectangular primary unit cell with the armchair (AC) and zigzag (ZZ) orientations orientated along the a and b vectors, respectively, is taken into consideration in order to model the uniaxial strain.The valence maximum and conduction minimum points of unstrained CuI were examined at Γ point for the rectangular brillouin zone and there is no shifting from the gamma point. At the same time, the direct band gap is not disturbed in the rectangular cell calculation. When uniaxial strain is applied in the AC orientation, the valance band maximum point is found at Γ. In calculations for rectangular supercell (2×4×1) CuI, a significant decrease is observed for pressure at %5 strain in ZZ orientation as shown in Fig.3.3(a). Therefore, a shift has occurred in the structure of the material. Afterwards, the pressure value continues up to %17. There is a sharp drop in pressure value at %20 strain. When the material is examined elastically, ruptures have started in its structure. The pressure value of the material after fracture is very close to the pressure value at %1 strain. As shown in Fig.3.3(b) AC orientation strain

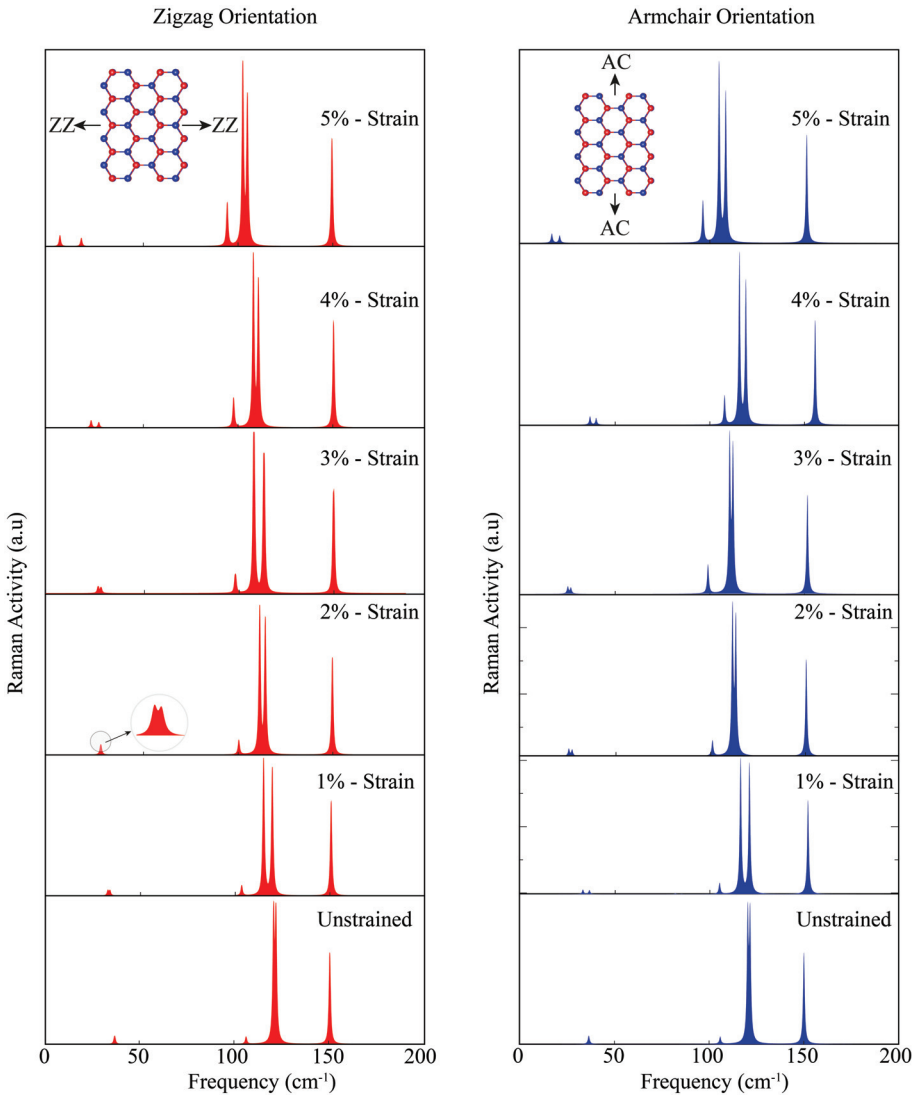

Figure 3.5. Strain dependent Raman spectrum of DLHC CuI

calculations were made up to %21. The highest pressure value was seen at %13 strain. While the sharp decrease in pressure was observed in %20 for AC direction, %21 strain was also observed in ZZ direction strain calculations and elastic rupture was also observed.

3.5. Conclusion

In conclusion, the structural, vibrational, electronic and mechanical properties of monolayer CuI crystals were calculated by density functional theory. The phonon band dispersion calculations reveal the dynamical stability of free-standing single-layer CuI which is found to possess four Raman active phonon modes in its vibrational spectrum. Structural optimization calculations showed that the lattice parameter of CuI is 4.08 Å. The fact that this value is the same in both axes of the material indicates that DLHC CuI has an isotropic structure. We compared lattice parameters for monolayer and bulk phases, lattice parameter of monolayer is lower than bulk phases. There are two different bond types between Cu and I as in-plane and out-of-plane. The charge transfer in the DLHC CuI structure is 0.3 electrons from the Cu atom to the I atom, as in the bulk phases. Also this result showed that the material has an ionic character. Local potential of the h-CuI structure was investigated and work function was found as 4.50 eV. This value is the same for both sides because the structure has a symmetrical geometry. Work function values of zincblende and wurtzite bulk phases were calculated as 2.19 eV and 2.72 eV, respectively. When the cohesive energies of DHLC CuI and bulk CuI are compared, the cohesive energy of monolayer CuI was calculated less than bulk phases. The electronic band dispersions showed that the single-layer CuI crystal has semiconductor nature with direct band gap which was calculated as 1.83 eV. The fact that the CuI has a direct band gap showed that it has the ability to luminescence. In addition, at the conduction band minimum and the valence band maximum points in the electronic band structure, the contribution of iodine atoms is dominant for electronic structure.

The effect of an external biaxial strain on the electronic band structure of CuI was investigated within a strain range from -5% to +5% and it showed that direct band gap behaviour does not change. We further investigated the elastic properties of single-layer CuI by means of both elastic and phononic instabilities under uniaxial tensile strains. It was found that in both zigzag and armchair orientations the elastic instabilities occur over the strain of 19% indicating the soft nature of CuI layer. In addition, the stress-strain curve along the ZZ direction reveal that single-layer CuI undergoes a structural phase transition between the 4% and 5% tensile uniaxial strains as indicated by a sudden drop of the stress in the lattice. Morever, the phonon band dispersions showed that the phononic

instability occurs at much smaller strain along the AC direction 8% than that of along the ZZ direction 14%. For ZZ and AC orientations, Raman calculations were performed for structures which have uniaxial strain from 0% to 5%. Strain calculations showed that the degenerate Raman active mode split as the amount of strain increased.

CHAPTER 4

OVERALL DISCUSSION

This master's thesis primarily used DFT-based first principles calculations to investigate and characterize an unique ultra-thin crystal type. This was motivated by the exceptional physics of electrons in low dimensions. A brief introduction about bulk and 2D materials is given in the first chapter, and the DFT approach is covered in the second chapter.

CuI is a novel 2D material that is suggested in the study from Chapter 3 and is both structurally and dynamically stable. Electronic band dispersions demonstrate that DLHC CuI is an direct band gap semiconductor with a tunable band gap which is changed by strain.

Through this thesis study, it was investigated how the electronic, magnetic, phononic, mechanical and chemical properties of an ultra-thin crystal structure can be calculated with the DFT method. Although the thesis work is focused on CuI, the experience gained here will be able to reliably realize the theoretical predictions of similar crystal structures.

REFERENCES

(1) Aapro, M., M. N. Huda, J. Karthikeyan, S. Kezilebieke, S. C. Ganguli, H. G. Herrero, X. Huang, P. Liljeroth, and H.-P. Komsa (2021). Synthesis and properties of monolayer mnse with unusual atomic structure and antiferromagnetic ordering. *ACS nano 15*(8), 13794–13802.

(2) Adamo, C. and V. Barone (1999). Toward reliable density functional methods without adjustable parameters: The pbe0 model. *The Journal of chemical physics 110*(13), 6158–6170.

(3) Ahmad, S. and S. Mukherjee (2014). A comparative study of electronic properties of bulk mos2 and its monolayer using dft technique: application of mechanical strain on mos2 monolayer.

(4) Ahn, K., G. H. Kim, S.-J. Kim, J. Kim, G.-S. Ryu, P. Lee, B. Ryu, J. Y. Cho, Y.-H. Kim, J. Kang, et al. (2022). Highly conductive p-type transparent conducting electrode with sulfur-doped copper iodide. *Chemistry of Materials 34*(23), 10517–10527.

(5) Alfè, D. (2009). Phon: A program to calculate phonons using the small displacement method. *Computer Physics Communications 180*(12), 2622–2633.

(6) Ang, P. K., W. Chen, A. T. S. Wee, and K. P. Loh (2008). Solution-gated epitaxial graphene as ph sensor. *Journal of the American Chemical Society 130*(44), 14392–14393.

(7) Archana, K., D. Yogalakshmi, and R. Rajagopal (2019). Application of green synthesized nanocrystalline cui in the removal of aqueous mn (vii) and cr (vi) ions. *SN Applied Sciences 1*, 1–14.

(8) Bafekry, A., M. Faraji, M. Fadlallah, H. Jappor, S. Karbasizadeh, M. Ghergherehchi, I. A. Sarsari, and A. A. Ziabari (2021). Novel two-dimensional alsb and insb monolayers with a double-layer honeycomb structure: a first-principles study. *Physical Chemistry Chemical Physics 23*(34), 18752–18759.

(9) Balandin, A. A., S. Ghosh, W. Bao, I. Calizo, D. Teweldebrhan, F. Miao, and C. N. Lau (2008). Superior thermal conductivity of single-layer graphene. *Nano letters 8*(3), 902–907.

(10) Balog, Á., G. F. Samu, P. V. Kamat, and C. Janáky (2019). Optoelectronic properties of cui photoelectrodes. *The Journal of Physical Chemistry Letters 10*(2), 259–264.

(11) Becke, A. D. (1988). Density-functional exchange-energy approximation with correct asymptotic behavior. *Physical review A 38*(6), 3098.

(12) Beeke, A. D. (1993). Density-functional thermochemistry. iii. the role of exact exchange. *J. Chem. Phys 98*(7), 5648–6.

(13) Beyer, M. K. (2000). The mechanical strength of a covalent bond calculated by density functional theory. *The Journal of Chemical Physics 112*(17), 7307–7312.

(14) Bonaccorso, F., Z. Sun, T. Hasan, and A. Ferrari (2010). Graphene photonics and optoelectronics. *Nature photonics 4*(9), 611–622.

(15) Ceperley, D. M. and B. J. Alder (1980). Ground state of the electron gas by a stochastic method. *Physical review letters 45*(7), 566.

(16) Chen, H., C.-Y. Wang, J.-T. Wang, Y. Wu, and S.-X. Zhou (2013). First-principles study of point defects in solar cell semiconductor cui. *Physica B: Condensed Matter 413*, 116–119.

(17) Choi, C.-H., J. Y. Gorecki, Z. Fang, M. Allen, S. Li, L.-Y. Lin, C.-C. Cheng, and C.-H. Chang (2016). Low-temperature, inkjet printed p-type copper (i) iodide thin film transistors. *Journal of Materials Chemistry C 4*(43), 10309–10314.

(18) Choi, S., Z. Shaolin, and W. Yang (2014). Layer-number-dependent work function of mos2 nanoflakes. *Journal of the Korean Physical Society 64*(10), 1550–1555.

(19) Ciofini, I. and C. A. Daul (2003). Dft calculations of molecular magnetic properties of coordination compounds. *Coordination Chemistry Reviews 238*, 187–209.

(20) Conesa-Egea, J., F. Zamora, and P. Amo-Ochoa (2019). Perspectives of the smart

cu-iodine coordination polymers: A portage to the world of new nanomaterials and composites. *Coordination Chemistry Reviews 381*, 65–78.

(21) Dappe, Y., R. Oszwaldowski, P. Pou, J. Ortega, R. Pérez, and F. Flores (2006). Local-orbital occupancy formulation of density functional theory: Application to si, c, and graphene. *Physical Review B 73*(23), 235124.

(22) Elias, D. C., R. R. Nair, T. Mohiuddin, S. Morozov, P. Blake, M. Halsall, A. C. Ferrari, D. Boukhvalov, M. Katsnelson, A. Geim, et al. (2009). Control of graphene's properties by reversible hydrogenation: evidence for graphane. *Science 323*(5914), 610–613.

(23) Ernzerhof, M. and G. E. Scuseria (1999). Assessment of the perdew–burke–ernzerhof exchange-correlation functional. *The Journal of chemical physics 110*(11), 5029–5036.

(24) Fakhree, A. A., Z. Ghasemi, M. Rahimi, and A. Shahrisa (2020). Enhanced catalytic performance of copper iodide in 1, 2, 3-triazole-imidazole hybrid synthesis, and evaluation of their anti-cancer activities along with optical properties besides 1h-tetrazole-imidazole hybrids. *Applied Organometallic Chemistry 34*(9), e5773.

(25) Fang, C., J. Zhang, X. Chen, and G. J. Weng (2020). Calculating the electrical conductivity of graphene nanoplatelet polymer composites by a monte carlo method. *Nanomaterials 10*(6), 1129.

(26) Gant, P., P. Huang, D. P. de Lara, D. Guo, R. Frisenda, and A. Castellanos-Gomez (2019). A strain tunable single-layer mos2 photodetector. *Materials Today 27*, 8–13.

(27) Geim, A. and K. Novoselov (2009). The rise of graphene, nanosci. *Technol. A Collect. Rev.. from Nat. Journals*, 11–19.

(28) Geim, A. K. and K. S. Novoselov (2010). The rise of graphene. In *Nanoscience and technology: a collection of reviews from nature journals*, pp. 11–19. World Scientific.

(29) Ghanbari, M. and M. Salavati-Niasari (2021). Copper iodide decorated graphitic carbon nitride sheets with enhanced visible-light response for photocatalytic organic pollutant removal and antibacterial activities. *Ecotoxicology and Environmental Safety 208*,

111712.

(30) Gomez De Arco, L., Y. Zhang, C. W. Schlenker, K. Ryu, M. E. Thompson, and C. Zhou (2010). Continuous, highly flexible, and transparent graphene films by chemical vapor deposition for organic photovoltaics. *ACS nano 4*(5), 2865–2873.

(31) Graužinytė, M., S. Botti, M. A. Marques, S. Goedecker, and J. A. Flores-Livas (2019). Computational acceleration of prospective dopant discovery in cuprous iodide. *Physical Chemistry Chemical Physics 21*(35), 18839–18849.

(32) Grimme, S., S. Ehrlich, and L. Goerigk (2011). Effect of the damping function in dispersion corrected density functional theory. *Journal of computational chemistry 32*(7), 1456–1465.

(33) Guo, Z., J. Li, R. Pan, J. Cheng, R. Chen, and T. He (2020). All-inorganic copper (i)-based ternary metal halides: promising materials toward optoelectronics. *Nanoscale 12*(29), 15560–15576.

(34) Hellman, H. and R. Feynman (1939). The operator method in quantum mechanics. *Physical Review 56*(7), 340–344.

(35) Heyd, J. and G. E. Scuseria (2004). Efficient hybrid density functional calculations in solids: Assessment of the heyd–scuseria–ernzerhof screened coulomb hybrid functional. *The Journal of chemical physics 121*(3), 1187–1192.

(36) Heyd, J., G. E. Scuseria, and M. Ernzerhof (2003). Hybrid functionals based on a screened coulomb potential. *The Journal of chemical physics 118*(18), 8207–8215.

(37) Hohenberg, P. and W. Kohn (1964). Inhomogeneous electron gas. *Physical review 136*(3B), B864.

(38) Jaschik, S., M. R. Marques, M. Seifert, C. Rodl, S. Botti, and M. A. Marques (2019). Stable ordered phases of cuprous iodide with complexes of copper vacancies. *Chemistry of Materials 31*(19), 7877–7882.

(39) Jiang, T., W. Sun, Q. Zhu, N. A. Burns, S. A. Khan, R. Mo, and Z. Gu (2015). Furin-mediated sequential delivery of anticancer cytokine and small-molecule drug

shuttled by graphene. *Advanced materials 27*(6), 1021–1028.

(40) Johan, M. R., K. Si-Wen, N. Hawari, and N. A. K. Aznan (2012). Synthesis and characterization of copper (i) iodide nanoparticles via chemical route. *Int. J. Electrochem. Sci 7*(6).

(41) Jönsson, J. (2020). *Electronic transitions and correlation effects: From pure elements to complex materials*, Volume 2053. Linköping University Electronic Press.

(42) Joseph, N., T. Sebastian, J. C. John, and S. Augustine (2020). Synthesis and characterization of sprayed copper iodide thin films on flexible substrate. In *AIP Conference Proceedings*, Volume 2263, pp. 050008. AIP Publishing LLC.

(43) Kadantsev, E. S. and P. Hawrylak (2012). Electronic structure of a single mos2 monolayer. *Solid state communications 152*(10), 909–913.

(44) Karthikeyan, V., V. C. Theja, M. M. De Souza, and V. A. Roy (2022). Hierarchically interlaced 2d copper iodide/mxene composite for high thermoelectric performance. *physica status solidi (RRL)–Rapid Research Letters 16*(1), 2100419.

(45) Kharche, N. and S. K. Nayak (2011). Quasiparticle band gap engineering of graphene and graphone on hexagonal boron nitride substrate. *Nano letters 11*(12), 5274–5278.

(46) Kim, K. S., Y. Zhao, H. Jang, S. Y. Lee, J. M. Kim, K. S. Kim, J.-H. Ahn, P. Kim, J.-Y. Choi, and B. H. Hong (2009). Large-scale pattern growth of graphene films for stretchable transparent electrodes. *nature 457*(7230), 706–710.

(47) Kohn, W. and L. J. Sham (1965). Self-consistent equations including exchange and correlation effects. *Physical review 140*(4A), A1133.

(48) Kravets, V., A. Grigorenko, R. Nair, P. Blake, S. Anissimova, K. Novoselov, and A. Geim (2010). Spectroscopic ellipsometry of graphene and an exciton-shifted van hove peak in absorption. *Physical Review B 81*(15), 155413.

(49) Kresse, G. and J. Furthmüller (1996). Efficient iterative schemes for ab initio total-energy calculations using a plane-wave basis set. *Physical review B 54*(16), 11169.

(50) Kresse, G., J. Furthmüller, and J. Hafner (1995). Ab initio force constant approach to phonon dispersion relations of diamond and graphite. *Europhysics Letters 32*(9), 729.

(51) Kresse, G. and J. Hafner (1993). Ab initio molecular dynamics for liquid metals. *Physical review B 47*(1), 558.

(52) Krukau, A. V., O. A. Vydrov, A. F. Izmaylov, and G. E. Scuseria (2006). Influence of the exchange screening parameter on the performance of screened hybrid functionals. *The Journal of chemical physics 125*(22), 224106.

(53) Kulkarni, G. S., K. Reddy, Z. Zhong, and X. Fan (2014). Graphene nanoelectronic heterodyne sensor for rapid and sensitive vapour detection. *Nature communications 5*(1), 4376.

(54) Lee, C., X. Wei, J. W. Kysar, and J. Hone (2008). Measurement of the elastic properties and intrinsic strength of monolayer graphene. *science 321*(5887), 385–388.

(55) Lee, C., W. Yang, and R. G. Parr (1988). Development of the colle-salvetti correlation-energy formula into a functional of the electron density. *Physical review B 37*(2), 785.

(56) Li, H., T. Liu, P. Wei, L. Lin, D. Gao, G. Wang, and X. Bao (2021). High-rate co2 electroreduction to c2+ products over a copper-copper iodide catalyst. *Angewandte Chemie 133*(26), 14450–14454.

(57) Li, Z. H., J. X. He, X. H. Lv, L. F. Chi, K. O. Egbo, M.-D. Li, T. Tanaka, Q. X. Guo, K. M. Yu, and C. P. Liu (2022). Optoelectronic properties and ultrafast carrier dynamics of copper iodide thin films. *Nature Communications 13*(1), 6346.

(58) Lin, Y.-M., C. Dimitrakopoulos, K. A. Jenkins, D. B. Farmer, H.-Y. Chiu, A. Grill, and P. Avouris (2010). 100-ghz transistors from wafer-scale epitaxial graphene. *Science 327*(5966), 662–662.

(59) Liu, J., L. Cui, and D. Losic (2013). Graphene and graphene oxide as new nanocarriers for drug delivery applications. *Acta biomaterialia 9*(12), 9243–9257.

(60) López, J., J. G. Platas, U. R. Rodríguez-Mendoza, J. I. Martinez, S. Delgado,

G. Lifante-Pedrola, E. Cantelar, R. Guerrero-Lemus, C. Hernandez-Rodriguez, and P. Amo-Ochoa (2020). Cu (i)–i-2, 4-diaminopyrimidine coordination polymers with optoelectronic properties as a proof of concept for solar cells. *Inorganic Chemistry 60*(2), 1208–1219.

(61) Luo, W., C. Zeng, X. Du, C. Leng, W. Yao, H. Shi, X. Wei, C. Du, and S. Lu (2018). Copper thiocyanate/copper iodide based hole transport composites with balanced properties for efficient polymer light-emitting diodes. *Journal of Materials Chemistry C 6*(18), 4895–4902.

(62) Ma, Y., Y. Dai, M. Guo, C. Niu, L. Yu, and B. Huang (2011). Strain-induced magnetic transitions in half-fluorinated single layers of bn, gan and graphene. *Nanoscale 3*(5), 2301–2306.

(63) Mahyavanshi, R. D., P. Desai, A. Ranade, M. Tanemura, and G. Kalita (2019). Observing charge transfer interaction in cui and mos2 heterojunction for photoresponsive device application. *ACS Applied Electronic Materials 1*(3), 302–310.

(64) Mallick, S., P. Mukhi, P. Kumari, K. R. Mahato, S. K. Verma, and D. Das (2019). Synthesis, characterization and catalytic application of starch supported cuprous iodide nanoparticles. *Catalysis Letters 149*, 3501–3507.

(65) Margolis, L. A., R. W. Schaeffer, and C. H. Yoder (2001). The synthesis and analysis of copper (i) iodide. a first-year laboratory project. *Journal of Chemical Education 78*(2), 235.

(66) Mayor-López, M. J. and J. Weber (1997). Dft calculations of the binding energy of metallocenes. *Chemical physics letters 281*(1-3), 226–232.

(67) Meftahi, A., M. Shabani-Nooshabadi, and A. Reisi-Vanani (2023). Introducing go/cui nanostructure as active electrode matter for supercapacitors: A comparative investigation within two aqueous electrolytes. *Journal of Energy Storage 63*, 107077.

(68) Mishra, D., K. Mokurala, A. Kumar, S. G. Seo, H. B. Jo, and S. H. Jin (2023). Light-mediated multi-level flexible copper iodide resistive random access memory for forming-free, ultra-low power data storage application. *Advanced Functional*

Materials 33(8), 2211022.

(69) Mo, R., T. Jiang, W. Sun, and Z. Gu (2015). Atp-responsive dna-graphene hybrid nanoaggregates for anticancer drug delivery. *Biomaterials 50*, 67–74.

(70) Mulla, R. and M. Rabinal (2018). Defect-controlled copper iodide: A promising and ecofriendly thermoelectric material. *Energy Technology 6*(6), 1178–1185.

(71) Mustonen, K., C. Hofer, P. Kotrusz, A. Markevich, M. Hulman, C. Mangler, T. Susi, T. J. Pennycook, K. Hricovini, C. Richter, et al. (2022). Toward exotic layered materials: 2d cuprous iodide. *Advanced Materials 34*(9), 2106922.

(72) Myeni, N., S. K. Ghosh, V. K. Perla, and K. Mallick (2019). Copper iodide nanoparticles within the organic matrix: An efficient catalyst for the electro-oxidation of formic acid. *Materials Research Express 6*(10), 1050a7.

(73) Nair, R. R., P. Blake, A. N. Grigorenko, K. S. Novoselov, T. J. Booth, T. Stauber, N. M. Peres, and A. K. Geim (2008). Fine structure constant defines visual transparency of graphene. *science 320*(5881), 1308–1308.

(74) Nair, R. R., W. Ren, R. Jalil, I. Riaz, V. G. Kravets, L. Britnell, P. Blake, F. Schedin, A. S. Mayorov, S. Yuan, et al. (2010). Fluorographene: a two-dimensional counterpart of teflon. *small 6*(24), 2877–2884.

(75) Neto, A. C., F. Guinea, N. M. Peres, K. S. Novoselov, and A. K. Geim (2009). The electronic properties of graphene. *Reviews of modern physics 81*(1), 109.

(76) Novoselov, K. S., A. K. Geim, S. V. Morozov, D. Jiang, M. I. Katsnelson, I. V. Grigorieva, S. Dubonos, and Firsov (2005). Two-dimensional gas of massless dirac fermions in graphene. *nature 438*(7065), 197–200.

(77) Novoselov, K. S., A. K. Geim, S. V. Morozov, D.-e. Jiang, Y. Zhang, S. V. Dubonos, I. V. Grigorieva, and A. A. Firsov (2004). Electric field effect in atomically thin carbon films. *science 306*(5696), 666–669.

(78) Papageorgiou, D. G., I. A. Kinloch, and R. J. Young (2017). Mechanical properties of graphene and graphene-based nanocomposites. *Progress in materials science 90*,

75–127.

(79) Perdew, J., K. Burke, and M. Ernzerhof (1996a). Generalized gradient approximation made simple. *Physical Review Letters 77*(18), 3865–3868.

(80) Perdew, J. P., K. Burke, and M. Ernzerhof (1996b). Generalized gradient approximation made simple. *Physical review letters 77*(18), 3865.

(81) Peres, N. M. (2010). Colloquium: The transport properties of graphene: An introduction. *Reviews of modern physics 82*(3), 2673.

(82) Qin, L., Z.-H. Zhang, Z. Jiang, K. Fan, W.-H. Zhang, Q.-Y. Tang, H.-N. Xia, F. Meng, Q. Zhang, L. Gu, et al. (2021). Realization of alsb in the double-layer honeycomb structure: A robust class of two-dimensional material. *ACS nano 15*(5), 8184–8191.

(83) Robinson, J. T., J. S. Burgess, C. E. Junkermeier, S. C. Badescu, T. L. Reinecke, F. K. Perkins, M. K. Zalalutdniov, J. W. Baldwin, J. C. Culbertson, P. E. Sheehan, et al. (2010). Properties of fluorinated graphene films. *Nano letters 10*(8), 3001–3005.

(84) Rochford, L. A., D. Keeble, O. Holmes, G. Clarkson, and T. Jones (2014). Controlling templating effects at the organic/inorganic interface using (111) oriented copper iodide. *Journal of Materials Chemistry C 2*(30), 6056–6060.

(85) Safaei-Ghomi, J., M. A. Ghasemzadeh, and A. Kakavand-Qalenoei (2016). Cui-nanoparticles-catalyzed one-pot synthesis of benzo [b] furans via three-component coupling of aldehydes, amines and alkyne. *Journal of Saudi Chemical Society 20*(5), 502–509.

(86) Serrano, J., M. Cardona, T. Ritter, B. Weinstein, A. Rubio, and C. Lin (2002). Pressure and temperature dependence of the raman phonons in isotopic γ-cui. *Physical Review B 66*(24), 245202.

(87) Sharma, G., T. Shanap, K. Patel, and M. El-Mansy (2012). Photovoltaic properties of bulk heterojunction devices based on cui-pva as electron donor and pcbm and modified pcbm as electron acceptor. *Materials Science-Poland 30*, 10–16.

(88) Sheha, E., H. Khoder, T. Shanap, M. El-Shaarawy, and M. El Mansy (2012). Structure,

dielectric and optical properties of p-type (pva/cui) nanocomposite polymer electrolyte for photovoltaic cells. *Optik 123*(13), 1161–1166.

(89) Shi, B., J. Jia, X. Feng, G. Ma, Y. Wu, and B. Cao (2021). Thermal evaporated cui film thickness-dependent performance of perovskite solar cells. *Vacuum 187*, 110076.

(90) Sofo, J. O., A. S. Chaudhari, and G. D. Barber (2007). Graphane: A two-dimensional hydrocarbon. *Physical Review B 75*(15), 153401.

(91) Splendiani, A., L. Sun, Y. Zhang, T. Li, J. Kim, C.-Y. Chim, G. Galli, and F. Wang (2010). Emerging photoluminescence in monolayer mos2. *Nano letters 10*(4), 1271–1275.

(92) Thomas, L. H. (1927). The calculation of atomic fields. In *Mathematical proceedings of the Cambridge philosophical society*, Volume 23, pp. 542–548. Cambridge University Press.

(93) Tkacz, R., R. Oldenbourg, S. B. Mehta, M. Miansari, A. Verma, and M. Majumder (2014). ph dependent isotropic to nematic phase transitions in graphene oxide dispersions reveal droplet liquid crystalline phases. *Chemical communications 50*(50), 6668–6671.

(94) Topkıran, U. C., Y. O. Yayak, M. Yagmurcukardes, et al. Van der waals heterostructures of single-layers of cui and inse: Electronic and vibrational properties.

(95) Viswanathan, A. and S. A. Suthanthiraraj (1993). Frequency response analysis of the fast ion conducting system cuprous iodide—silver chromate. *Materials research bulletin 28*(8), 821–828.

(96) Vlček Jr, A. and S. Záliš (2007). Modeling of charge-transfer transitions and excited states in d6 transition metal complexes by dft techniques. *Coordination chemistry reviews 251*(3-4), 258–287.

(97) Vora-ud, A., K. Chaarmart, W. Kasemsin, S. Boonkirdram, and T. Seetawan (2022). Transparent thermoelectric properties of copper iodide thin films. *Physica B: Condensed Matter 625*, 413527.

(98) Wang, X., A. Liu, Y. Xing, H. Duan, W. Xu, Q. Zhou, H. Wu, C. Chen, and B. Chen (2018). Three-dimensional graphene biointerface with extremely high sensitivity to single cancer cell monitoring. *Biosensors and Bioelectronics 105*, 22–28.

(99) Wang, Y., L. Wang, T. Yang, X. Li, X. Zang, M. Zhu, K. Wang, D. Wu, and H. Zhu (2014). Wearable and highly sensitive graphene strain sensors for human motion monitoring. *Advanced Functional Materials 24*(29), 4666–4670.

(100) Wu, J., H. A. Becerril, Z. Bao, Z. Liu, Y. Chen, and P. Peumans (2008). Organic solar cells with solution-processed graphene transparent electrodes. *Applied physics letters 92*(26).

(101) Wu, J., P. Cao, Z. Zhang, F. Ning, S.-s. Zheng, J. He, and Z. Zhang (2018). Grain-size-controlled mechanical properties of polycrystalline monolayer mos2. *Nano letters 18*(2), 1543–1552.

(102) Xia, F., T. Mueller, Y.-m. Lin, A. Valdes-Garcia, and P. Avouris (2009). Ultrafast graphene photodetector. *Nature nanotechnology 4*(12), 839–843.

(103) Xu, J., A. Chen, L. Yu, D. Wei, Q. Tian, H. Wang, Z. Qin, and G. Qin (2022). The record low thermal conductivity of monolayer cuprous iodide (cui) with a direct wide bandgap. *Nanoscale 14*(46), 17401–17408.

(104) Xu, S., J. Zhan, B. Man, S. Jiang, W. Yue, S. Gao, C. Guo, H. Liu, Z. Li, J. Wang, et al. (2017). Real-time reliable determination of binding kinetics of dna hybridization using a multi-channel graphene biosensor. *Nature communications 8*(1), 14902.

(105) Yakovleva, G., A. Berdinsky, A. Romanenko, S. Khabarov, and V. E. Fedorov (2015). The conductivity and temf of mos 2 with mo 2 s 3 additive. In *2015 38th International Convention on Information and Communication Technology, Electronics and Microelectronics (MIPRO)*, pp. 12–14. IEEE.

(106) Yang, C., M. Kneiß, F.-L. Schein, M. Lorenz, and M. Grundmann (2016). Room-temperature domain-epitaxy of copper iodide thin films for transparent cui/zno heterojunctions with high rectification ratios larger than 109. *Scientific reports 6*(1), 21937.

(107) Yang, C., E. Rose, W. Yu, T. Stralka, F. Geng, M. Lorenz, and M. Grundmann (2020). Controllable growth of copper iodide for high-mobility thin films and self-assembled microcrystals. *ACS Applied Electronic Materials 2*(11), 3627–3632.

(108) Yang, K., L. Feng, and Z. Liu (2016). Stimuli responsive drug delivery systems based on nano-graphene for cancer therapy. *Advanced drug delivery reviews 105*, 228–241.

(109) Yao, K., P. Chen, Z. Zhang, J. Li, R. Ai, H. Ma, B. Zhao, G. Sun, R. Wu, X. Tang, et al. (2018). Synthesis of ultrathin two-dimensional nanosheets and van der waals heterostructures from non-layered γ-cui. *npj 2D Materials and Applications 2*(1), 16.

(110) Yoon, H. J., J. H. Yang, Z. Zhou, S. S. Yang, M. M.-C. Cheng, et al. (2011). Carbon dioxide gas sensor using a graphene sheet. *Sensors and Actuators B: Chemical 157*(1), 310–313.

(111) Yu, Y.-J., Y. Zhao, S. Ryu, L. E. Brus, K. S. Kim, and P. Kim (2009). Tuning the graphene work function by electric field effect. *Nano letters 9*(10), 3430–3434.

(112) Zhou, J., Q. Wang, Q. Sun, X. Chen, Y. Kawazoe, and P. Jena (2009). Ferromagnetism in semihydrogenated graphene sheet. *Nano letters 9*(11), 3867–3870.

(113) Zhu, K., Z. Cheng, S. Rangan, M. Cotlet, J. Du, L. Kasaei, S. J. Teat, W. Liu, Y. Chen, L. C. Feldman, et al. (2021). A new type of hybrid copper iodide as nontoxic and ultrastable led emissive layer material. *ACS Energy Letters 6*(7), 2565–2574.

(114) Zhu, Y., S. Murali, M. D. Stoller, K. J. Ganesh, W. Cai, P. J. Ferreira, A. Pirkle, R. M. Wallace, K. A. Cychosz, M. Thommes, et al. (2011). Carbon-based supercapacitors produced by activation of graphene. *science 332*(6037), 1537–1541.